Dependencies of Four Mechanisms of Secondary Ice Production on Cloud-Top Temperature in a Continental Convective Storm

DEEPAK WAMAN,[a] SACHIN PATADE,[a] ARTI JADAV,[a] AKASH DESHMUKH,[a] ASHOK KUMAR GUPTA,[a,b] VAUGHAN T. J. PHILLIPS,[a] AARON BANSEMER,[c] AND PAUL J. DEMOTT[d]

[a] *Department of Physical Geography and Ecosystem Science, Lund University, Lund, Sweden*
[b] *Department of Earth and Environmental Sciences, Vanderbilt University, Nashville, Tennessee*
[c] *Mesoscale and Microscale Meteorology Laboratory, National Center for Atmospheric Research, Boulder, Colorado*
[d] *Department of Atmospheric Science, Colorado State University, Fort Collins, Colorado*

(Manuscript received 27 October 2021, in final form 28 June 2022)

ABSTRACT: Various mechanisms of secondary ice production (SIP) cause multiplication of numbers of ice particle, after the onset of primary ice. A measure of SIP is the ice enhancement ratio ("IE ratio") defined here as the ratio between number concentrations of total ice (excluding homogeneously nucleated ice) and active ice-nucleating particles (INPs). A convective line observed on 11 May 2011 over the Southern Great Plains in the Mesoscale Continental Convective Cloud Experiment (MC3E) campaign was simulated with the "Aerosol–Cloud" (AC) model. AC is validated against coincident MC3E observations by aircraft, ground-based instruments, and satellite. Four SIP mechanisms are represented in AC: the Hallett–Mossop (HM) process of rime splintering, and fragmentation during ice–ice collisions, raindrop freezing, and sublimation. The vertical profile of the IE ratio, averaged over the entire simulation, is almost uniform (10^2 to 10^3) because fragmentation in ice–ice collisions dominates at long time scales, driving the ice concentration toward a theoretical maximum. The IE ratio increases with both the updraft (HM process, fragmentation during raindrop freezing, and ice–ice collisions) and downdraft speed (fragmentation during ice–ice collisions and sublimation). As reported historically in aircraft sampling, IE ratios were predicted to peak near 10^3 for cloud-top temperatures close to the −12°C level, mostly due to the HM process in typically young clouds with their age less than 15 min. At higher altitudes with temperatures of −20° to −30°C, the predicted IE ratios were smaller, ranging from 10 to 10^2, and mainly resulted from fragmentation in ice–ice collisions.

KEYWORDS: Aerosols; Cloud microphysics; Ice particles; Clouds

1. Introduction

Hydrometeors in the atmosphere are either liquid or ice. Ice particles in clouds affect precipitation, radiative transfer, and cloud electrification (Rangno and Hobbs 2001; Cantrell and Heymsfield 2005). Mechanisms of ice initiation, which remain uncertain (Cantrell and Heymsfield 2005; Field et al. 2017), are fundamental for the climate. Precipitation globally is associated with the ice phase (Field and Heymsfield 2015) and controls cloud extent.

There are two possible mechanisms for precipitation production, and one of these is the "ice-crystal process," which involves the vapor growth of ice crystals to form snow (Yau and Rogers 1996). This snow may rime to form graupel which might subsequently melt to form ("cold") rain. The other process for precipitation formation involves the coalescence of cloud droplets to form "warm" rain ("warm rain process"), which may precipitate on its own, or freeze to form graupel that may also subsequently melt (e.g., Phillips et al. 2001; Sun et al. 2012). Note that the terms "warm" and "cold" applied to precipitation do not refer to its temperature but rather to its mechanism of origin.

Above the freezing level, formation of the first ("primary") ice requires activity of ice-nucleating particles (INPs) for precipitating clouds with tops warmer than −36°C. Active INPs are rare with concentrations typically between about 10^{-5} and 1 L^{-1} near −10°C (Hobbs 1969; DeMott et al. 2003; Möhler et al. 2005; Lasher-Trapp et al. 2016). It is commonly observed that in natural convective clouds with tops warmer than about −36°C, concentrations of ice are up to a factor of 10^4 higher than those of available active INPs (e.g., Harris-Hobbs and Cooper 1987; Jackson et al. 2018; Lasher-Trapp et al. 2021). For example, with modern optical probes and processing algorithms that eliminate any bias from artificial shattering (Field et al. 2006; Korolev et al. 2011), Ladino et al. (2017) observed that the discrepancy between number concentrations of active INP and total ice remains. Several similarly accurate studies of tropical cumulus clouds such as those by Lawson et al. (2015), Lasher-Trapp et al. (2016, 2021), and Huang et al. (2017) reported rapid glaciation in clouds with tops much warmer than ~−18°C, with abundant ice.

It has long been proposed that some processes must exist following initial primary ice nucleation to enhance the number and mass concentration of ice. Such processes are termed "secondary ice production" (SIP) mechanisms (Langmuir 1948; Hobbs 1969). They are envisaged to create positive feedbacks with growth of fragments to form fragmenting precipitation ("ice multiplication"). In a recent study, Zhao and Liu (2021) included various SIP mechanisms in a global climate model with improved simulation of liquid and ice water paths. SIP mechanisms can alter the cloud properties, such as precipitation rate, cloud lifetime, glaciation, and electrification (e.g., Crawford et al. 2012; Lawson et al. 2015; Lasher-Trapp et al. 2016, 2021;

Corresponding author: Deepak Waman, deepak.waman@nateko.lu.se

DOI: 10.1175/JAS-D-21-0278.1

Phillips et al. 2017b, 2018, 2020; Sotiropoulou et al. 2021; Georgakaki et al. 2022).

Secondary ice production mechanisms

Various known SIP mechanisms in natural clouds depend on parameters such as vertical velocity, temperature, and particle size distributions (PSDs). As reviewed by Field et al. (2017), there are several possible SIP mechanisms:

1) The Hallett–Mossop ("HM"; Hallett and Mossop 1974) process of rime splintering
2) Fragmentation during ice–ice collisions (Vardiman 1978; Takahashi et al. 1995)
3) Shattering of freezing rain or drizzle, also including that of incident branched crystals in drop–ice collisions (e.g., Dye and Hobbs 1968)
4) Fragmentation during sublimation (e.g., Oraltay and Hallett 1989)
5) SIP production due to activation of INPs during transient fluctuations of supersaturation in wakes of warm precipitation particles (e.g., Prabhakaran et al. 2019)

The HM process is one of several known SIP mechanisms in which small ice splinters break away during riming of supercooled cloud droplets > 24 μm, for the temperature range of $-3°$ to $-8°$C. At temperatures warmer than $-3°$C supercooled droplets do not form an ice shell (Dong and Hallett 1989). When colder than $-8°$C, their ice shells are hard to break by the internal pressure (Griggs and Choularton 1983). Field observations (Harris-Hobbs and Cooper 1987; Blyth and Latham 1993; Patade et al. 2016; Jackson et al. 2018; Lasher-Trapp et al. 2021) and numerical modeling (Blyth and Latham 1997; Huang et al. 2017; Gayatri et al. 2022; Lasher-Trapp et al. 2021) of cumulus clouds with warm cloud tops ($>-20°$C) showed that HM process can account for the observed high concentration of ice.

Yet several laboratory and field studies (Vardiman 1978; Takahashi et al. 1995; reviewed by Phillips et al. 2017a,b, 2021) have observed the fragmentation of ice particles in collisions. Takahashi et al. (1995) measured maximum ice production from ice–ice collisions at about $-16°$C. From field observations, Hobbs (1972) concluded that fragmentation in graupel–dendrite collisions might cause ice enhancement. Modeling studies such as those by Fridlind et al. (2007) (crystal–crystal collision), Yano and Phillips (2011) (graupel–graupel collisions), Phillips et al. (2017a) (all ice–ice collisions involving crystal, snow, and graupel), Sotiropoulou et al. (2021), and Zhao et al. (2021) reported fragmentation during ice–ice collisions. To simulate SIP during any ice–ice collision, Phillips et al. (2017a,b) developed a theoretical formulation based on the principle of energy conservation. The number of secondary fragments from a collision depends on the initial kinetic energy and habits of the colliding ice particles, which depend on factors such as temperature, particle size, and riming intensity of ice particles.

Another SIP mechanism active in clouds is shattering of freezing rain or drizzle, as seen in laboratory studies (Johnson and Hallett 1968; Pruppacher and Schlamp 1975; Leisner et al. 2014; Keinert et al. 2020). The liquid may get trapped inside an ice shell during raindrop freezing. Due to the density difference of ice and water, the excess pressure builds up in the trapped water, and if it exceeds a threshold during freezing, the external ice shell breaks, and spikes and fragments may get emitted. Aircraft observations by Rangno (2008) and Lawson et al. (2015) of frozen fragments of ice were consistent with fracturing of frozen raindrops. Phillips et al. (2018) provided an empirical formulation for secondary fragments from raindrop freezing, using laboratory observations only of drops in free-fall [section 2b(2)]. No laboratory observations of electrodynamically levitated drops were used, as Phillips et al. (2018) argued that the natural fall behavior governs the spherical symmetry of latent heat loss to the air, the ice shell geometry and hence the fragmentation in real clouds. Keinert et al. (2020) confirmed this.

Another idea is that ice formation upon collision of an ice crystal with a supercooled raindrop is seen to cause a breakup of the crystal (Dye and Hobbs 1968; King and Fletcher 1976a,b). We view this as an aspect of raindrop freezing fragmentation. It is already implicitly treated in part by our raindrop freezing fragmentation scheme (Phillips et al. 2018) since it is based on laboratory observations of raindrops that partly freeze in collisions with ice crystals. However, this process is not yet well understood.

Ice multiplication may also occur during sublimation of ice particles in subsaturated cloudy regions, as seen in laboratory studies (Oraltay and Hallett 1989; Dong et al. 1994; Bacon et al. 1998). Oraltay and Hallett (1989) observed that when the relative humidity over ice (RH_i) is less than 70% at subzero temperature, dendritic ice crystals break up. Dong et al. (1994) observed fragmentation of rimed ice particles during sublimation. Deshmukh et al. (2022) formulated fragmentation during the sublimation of dendritic crystals and rimed ice particles such as graupel based on these laboratory studies. Sublimation breakup can be significant in deep convective descent (Deshmukh et al. 2022).

Activation of preexisting INPs (Prabhakaran et al. 2019) in transient supersaturations in the wake of a warm falling hydrometeor, has been hypothesized in view of laboratory observations of activation of cloud condensation nuclei (CCN) (Prabhakaran et al. 2020) and numerical modeling of supersaturation fluctuations (Chouippe et al. 2019). We have chosen not to represent this mechanism since any high humidity above water saturation would first initiate a droplet around the INP, only activating it in a freezing mode. The high ambient relative humidity would then be expected to become irrelevant to the ice nucleation.

Aircraft observations of nimbostratus clouds over China by Yang et al. (2014) proposed several SIP mechanisms (the HM process, fragmentation in ice–ice collisions, raindrop freezing fragmentation) responsible for high ice particle number concentrations in such clouds. They showed that between $-10°$ and $-15°$C levels, the prominent SIP mechanism was likely dendritic crystal–crystal collisions. Images of irregularly shaped ice crystals between $-3°$ and $-10°$C suggested that drizzle/rain shattering along with the HM process are prolific.

Lawson et al. (2015) and Phillips et al. (2018) suggested that raindrop freezing fragmentation and the HM process could explain the rapid glaciation in tropical cumulus clouds with broad drop size distribution (DSD). By simulating the

HM process and fragmentation in ice–ice collisions, Sullivan et al. (2017) predicted the enhancement in number concentrations of ice particles by up to 10^4 relative to all ice from INP activity and delineated that the maximum ice enhancement occurred at moderate ascent speeds and moderate aerosol loadings. The study by Zhao et al. (2021) suggested that the dominant SIP mechanism in Arctic mixed-phase clouds is fragmentation during freezing of raindrops. This suggests that the role of each SIP mechanism in producing high ice number concentrations varies greatly with cloud types.

A major challenge for successful representation of cloud microphysical properties is the accurate prediction of number concentrations of ice particles by inclusion of SIP. Recent cloud models can predict two moments of the size distribution (both mass and number mixing ratio), and the most advanced discretize it with bins. SIP has received less attention than heterogeneous ice nucleation (Pruppacher and Klett 1997, hereafter PK97; Field et al. 2017).

The term we use here to quantify the effect of SIP on overall ice concentrations is "ice enhancement (IE) ratio." Hobbs et al. (1980, hereafter H80) defined as the ratio of the average ice concentration at any in-cloud level to the concentration of INPs active at cloud top. Figure 1 shows the IE ratio observed by the aircraft from H80, averaged for small cumulus, cumulus complexes, and embedded cumulus clouds. The geometric mean of the plotted IE ratios can be as large as 10^4 to 10^5 and generally decreases with decreasing cloud-top temperatures aloft, with a slight peak near −12°C.

The Optical Array Probe (OAP) has been widely used to measure sizes and concentrations of ice particles over the decades. Such aircraft probes have been biased by artificial shattering on impact, generating numerous tiny ice crystals less than 100 μm. Field et al. (2006) showed that short interarrival times indicate artificially fragmented ice particles. Korolev et al. (2011) made observations by mounting both shatter-corrected and unmodified probes on the same flight. It was observed that the artificial fragmentation was prone in ice particles smaller than 0.2–0.5 mm. Instead of OAPs, H80 used a formvar particle sampler typically mounted in a long decelerator tube (~1 m × 0.1 m) to minimize any shattering bias (Hobbs et al. 1971). However, it is unknown whether any shattering bias contaminated their data (Fig. 1). Also, there was less understanding then of contamination issues in measuring active INP concentrations with filter papers (H80).

Considering the uncertainties in the relationship between ice enhancement and cloud-top temperature in such observations, it is vital to investigate the role of various SIP mechanisms in ice enhancement using model simulations. Here we present a modeling study of continental, deep convective clouds to investigate the role of four SIP mechanisms (the HM process of rime splintering, and fragmentation during raindrop freezing, ice–ice collisions, and sublimation) in ice enhancement using the Aerosol–Cloud (AC) model. To our knowledge, this is the first time that all four SIP mechanisms have been included in a cloud model. Using AC, we also investigated the dependency of ice production from these SIP mechanisms on cloud-top temperature. This study elucidates the time evolution of activities of the four SIP mechanisms and their onset

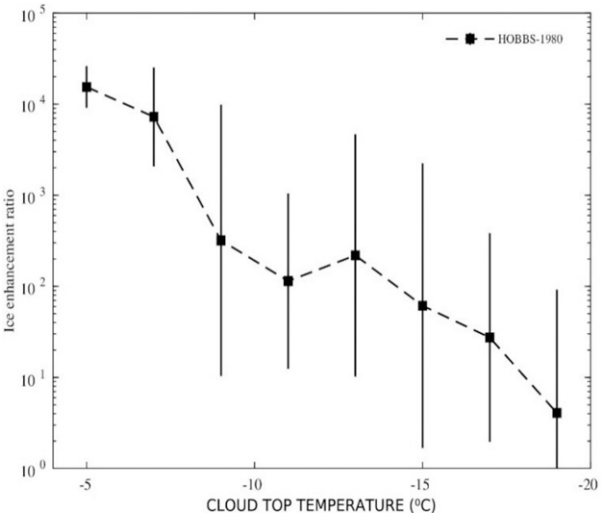

FIG. 1. Ice enhancement ratio (geometric mean), as a function of cloud-top temperature for updraft region (from H80, with changes).

times in the deep convection. Whereas a few earlier studies have observed SIP in maritime convective clouds (e.g., Heymsfield and Willis 2014; Lawson et al. 2015; Lloyd et al. 2020), the present study is focused solely on continental convective clouds.

2. Description of field campaign and observations

a. *Description of case*

The Midlatitude Continental Convective Cloud Experiment (MC3E) project was jointly led by the U.S. Department of Energy (DOE) Atmospheric Radiation Measurements (ARM) program and the National Aeronautics and Space Administration's (NASA) Global Precipitation Measurement (GPM) mission. It made observations for a total of 15 data missions focusing at and around the DOE ARM, Southern Great Plains (SGP) Central Facility (CF), and in north-central Oklahoma from 22 April to 6 June 2011. Data were collected from airborne and ground-based measurement (Jensen et al. 2016).

The Real-Time Mission Monitor (RTMM; Blakeslee et al. 2007) image (Fig. 2a) shows a radar picture of the simulated mesoscale convective system (MCS). The MCS was moving to the northeast (Jensen et al. 2016). The Citation aircraft sampled cloud bases only at takeoff and landing, mostly targeting the trailing stratiform region of the MCS. The aircraft observations were preliminary taken between 1800 and 2100 UTC as the system moved to the trailing stratiform mode as it passed over the CF (Jensen et al. 2016).

Figure 3 shows the observed profiles of initial air and dewpoint temperatures at 0000 UTC 10 May 2011. The lifting condensation level (LCL) was at 796 hPa. The case simulated here is the line of convective clouds observed in MC3E from 0900 to 2400 UTC 11 May 2011. It consisted of many cloud types, with deep convective clouds (e.g., cumulonimbi) with depths of 9–13 km and stratiform clouds. Convective clouds had relatively warm bases (~17°C) at about 1.5 km altitude above mean sea level (MSL). The ground level was about 350 m MSL. The case

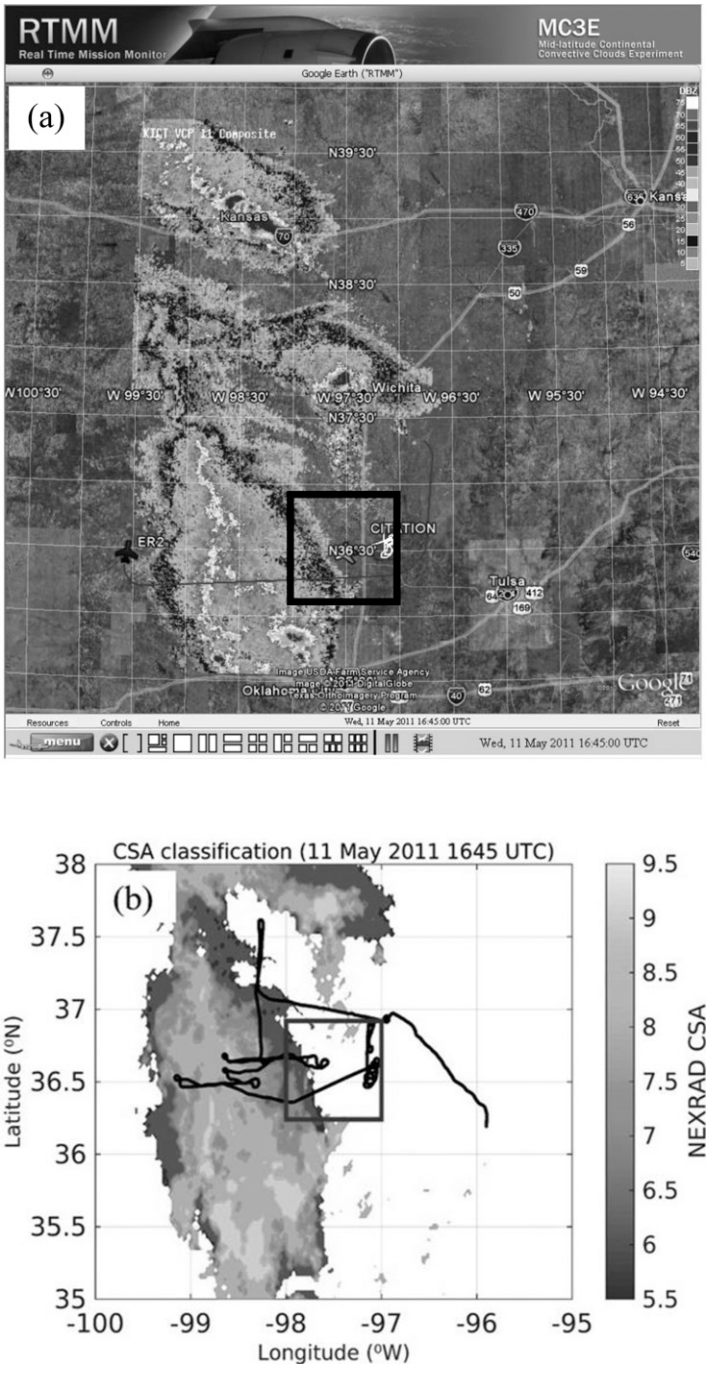

FIG. 2. (a) RTMM image during MC3E field campaign showing a plan position indicator of radar reflectivity from KICT radar at 1645 UTC with flight positions of citation (white line) and ER-2 aircraft (red line) (adapted from https://ghrc.nasa.gov/hydro), (b) convective–stratiform–anvil (CSA)-classified deep convective systems and Citation aircraft flight track (plotted for the entire flight duration, black line) superimposed on it for the simulated day of the MC3E at 1645 UTC. The CSA classification is based on Feng et al. (2011) (thick anvil: 5.5–7.5; stratiform: 7.5–8.5; convective: 8.5–9.5). The black boxes in (a) and (b) indicate the simulation domain.

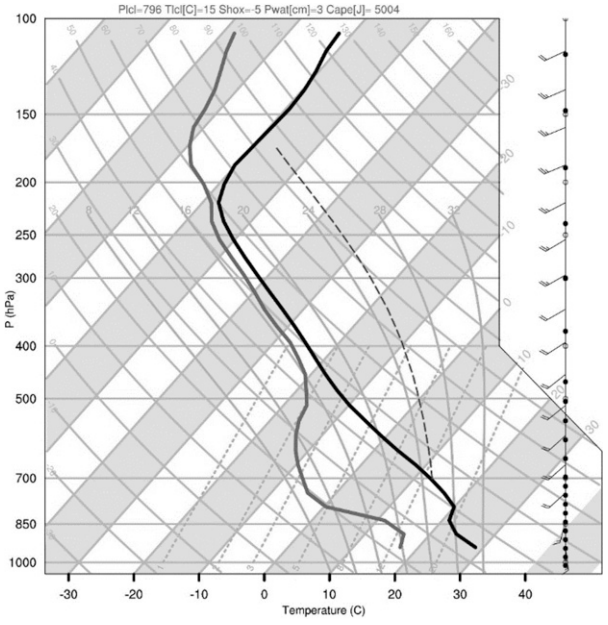

FIG. 3. Initial vertical dewpoint and temperature profiles at 0000 UTC 10 May 2011. A solid gray line represents the dewpoint, and a solid black line represents the air temperature. The thin dotted gray line indicates the moist adiabat.

had a high convective available potential energy (CAPE) (4000–5000 J kg^{-1}, Fig. 3) near the beginning of the simulated period (after 0000 UTC 10 May) when the lower troposphere was moistened by large-scale advection.

1) AIRBORNE MEASUREMENTS

Figures 2a and 2b show flight tracks of NASA ER-2 (red) and University of North Dakota (UND) Cessna Citation II (black) jet aircraft which were operational at 1645 UTC 11 May 2011 during the MC3E campaign. The optical probes (Table 1) carried by the UND Citation aircraft made measurements of in-cloud ice number concentrations, liquid water content (LWC), drop size and concentrations at altitudes between melting level and cloud top (~4–13 km).

The size and concentrations of droplets and LWC were measured by the cloud droplet probe (CDP). The Nevzorov and King hot-wire probes also measured the LWC during the MC3E campaign. However, these two probes were sensitive to ice in subsaturated regions, and conceivably also to any rain at warmer levels, so both probes were not used at all in the present study.

Moreover, the 2D cloud probe (2DC), cloud imaging probe (CIP), and high-volume precipitation spectrometer, version 3 (HVPS-3) were used to measure the ice concentration (Table 1). The combine spectrum ("COMB") uses the 2DC (or CIP) PSDs merged with the HVPS-3. During the aircraft measurements in MC3E, the 2DC and the HVPS-3 probes had "shattering corrected" tips, while the CIP was without any such antishatter tips. The 2DC and CIP probes used during the MC3E campaign were not able to measure particle size

TABLE 1. Instruments mounted on the Citation aircraft (Jensen et al. 2016).

Instrument	Range used
2DC	0.2–1.0 mm
CIP	0.2–1.5 mm
HVPS-3	0.2–19.2 mm
CDP	2–20 μm

and concentration in the size range of 50–200 μm accurately due to their coarse resolution (about 30 μm per pixel). To minimize the shattering of ice on the aircraft probes, shattered particles were identified and removed following the method described by Field et al. (2006) and Korolev et al. (2011). Only ice particles with a maximum size dimension >200 μm (NI_{200}) were included in plotted ice concentrations both in the simulation and observations to minimize any further shattering bias. However, in rest of the manuscript (other than model validation) the number concentrations of simulated ice include particles of all size ranges.

Furthermore, from Table 1, the impression that there is a measurement gap between particles of diameters between 50 (CDP maximum size) and 200 μm (2DC minimum size used). However, the coarse resolution of these probes and splashing of drops and shattering of ice can leave large uncertainties in the size range of 50–200 μm. Furthermore, the MC3E campaign did not use the Two-Dimensional Stereo (2DS) probe which could have measured particles in this size range, reasonably with 10 μm resolution. In addition to this, there are two extra sources of uncertainties associated with these probes i.e., optical response (since most of the small particles are out of focus) and electronic response. Though the limitation is there for measuring small particles, these optical probes (2DC and CIP) are still capable of measuring particles larger than 200 μm and most of the ice mass in convective clouds is typically in the larger size ranges (>200 μm). Moreover, the unfiltered 2DC size distribution plotted at levels near cloud base is consistent with that expected from the CDP size distribution (not shown here).

The Geostationary Operational Environmental Satellite (GOES) and Visible Infrared Solar-Infrared Split-Window Technique (VISST) measured the radiative fluxes at the top of the atmosphere (TOA).

Figure 4 shows PSD and corresponding images from the 2DC, CIP, and HVPS-3 probes at different in-cloud levels. The PSD changes from the cloud base (~17°C) to the upper half of the mixed-phase region, and corresponding images from the 2DC, CIP, and HVPS-3 probes at different in-cloud levels are shown in Fig. 4. Particles smaller than 200 μm are omitted from the PSDs because of the possibility of spurious fragments from artificial shattering on impact with the aircraft probes, which the antishatter tips might not fully eliminate (Field et al. 2006; Korolev et al. 2011) and poor time response of these probes at those smaller sizes (Gurganus and Lawson 2018). From these images (Figs. 4b,d), it can be seen that average size of particles (<1 mm) generally increases with height above cloud base (17°C) up to the −20°C level. The

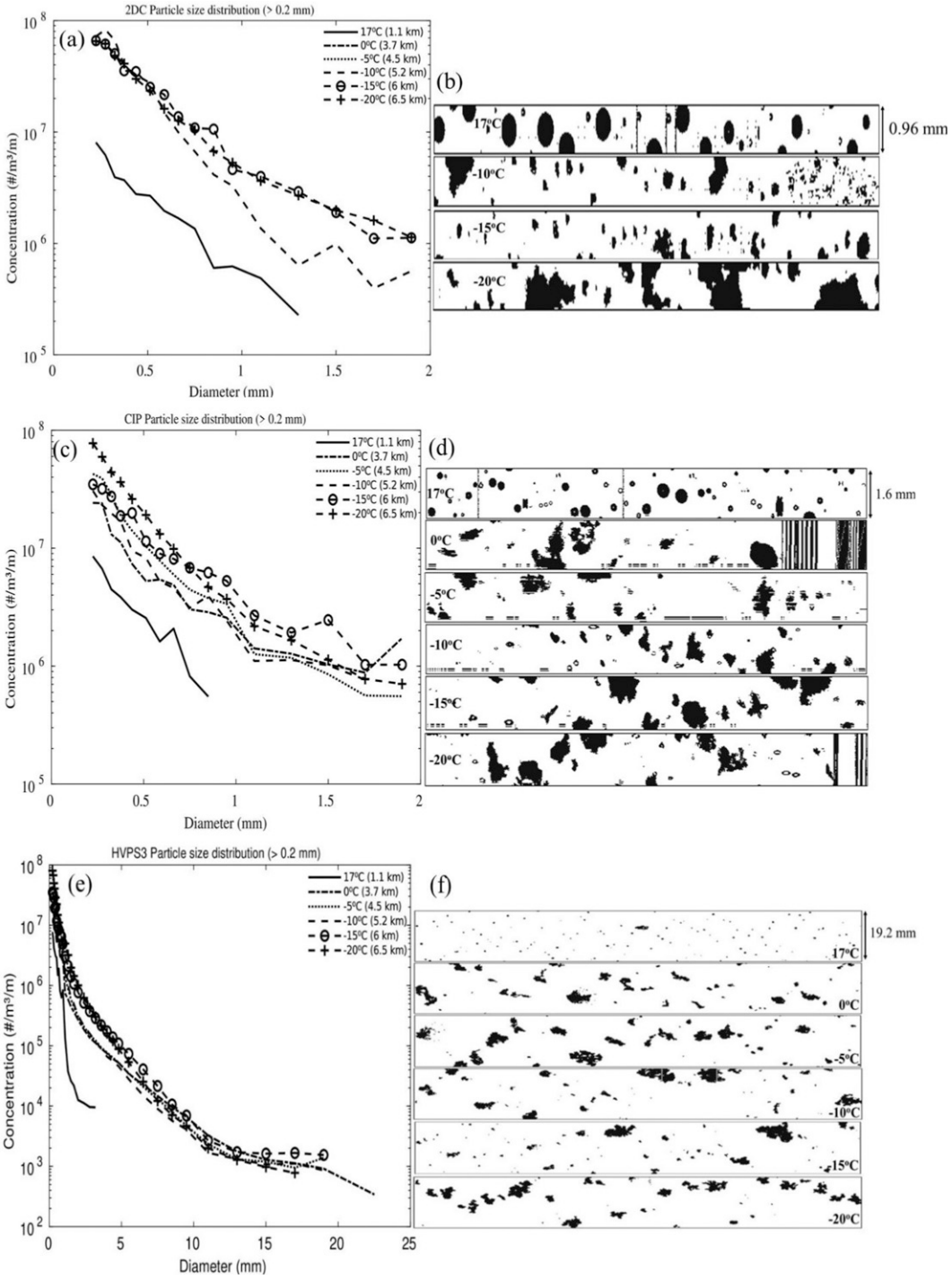

FIG. 4. (left) Particle size distribution for particles bigger than 0.2 mm and (right) corresponding images at various in-cloud levels from the (a),(b) 2DC, (c),(d) CIP, and (e),(f) HVPS3 probes on 11 May 2011 during MC3E.

warmest levels displayed correspond to mostly convective clouds whereas the colder levels are dominated by stratiform clouds.

Good agreement can be seen between PSDs from the 2DC probe (Fig. 4a) and CIP (Fig. 4c) for overlapping size bins. The PSD generally broadens with decreasing subzero temperature, indicating numerous larger ice particles near the cloud top. There was the presence of raindrops (0.5 to 1 mm) near the cloud base as observed by the 2DC imagery. The 2DC and CIP images show the presence of aggregates and rimed

ice particles of diameter about 1 mm at levels colder than −15°C. Pristine ice crystals with diameters greater than 0.5 mm were relatively rare in the 2DC and CIP imagery, indicating the dominance of ice crystal growth by riming. Also, PSDs reveals that only ice particles are present among all detected particles bigger than 200 μm above the freezing level.

2) GROUND-BASED MEASUREMENTS

During the MC3E campaign, the CCN number concentration was measured by a CCN counter at seven supersaturation levels (Jefferson 2011; Uin 2016) at Lamont, Oklahoma (~300 m MSL). The predicted radar reflectivity is compared with the reflectivity measured by the Ka-band ARM zenith radar (KAZR).

Large-scale advective tendencies of heat and moisture ("large-scale forcing"), and the surface heat and moisture fluxes were all derived from the measurements by constrained variational analysis (Jensen et al. 2016). However, these advective tendencies might be biased due to advection of layer clouds in the simulated region, likely from the remote source, as Jensen et al. (2016) reported the presence of widespread stratiform clouds in the first peak (1800–2400 UTC 10 May). The presence of this layer cloud was not measured directly in the MC3E sounding, from which the large-scale forcing was derived.

b. *Description of numerical model*

This study used AC, and it has been previously used extensively (e.g., Phillips et al. 2017b, 2018, 2020).

AC represents clouds and aerosols with hybrid spectral bin–two-moment bulk microphysics, interactive radiation, and semiprognostic aerosol schemes (Phillips et al. 2007, 2009, 2017, 2020; Kudzotsa et al. 2016). AC uses emulated bin microphysics schemes to treat various microphysical processes such as homogeneous and primary ice initiation, SIP processes, and droplet activation (Phillips et al. 2007, 2008, 2009, 2013, 2015, 2017, 2018). The Weather Research and Forecasting (WRF) Model framework was used as a dynamical basis for schemes such as planetary boundary layer (PBL), dynamics, surface layer, and subgrid-scale mixing. AC follows the "two-moment" approach in which the total mass and number of each microphysical species are diffused and advected as bulk prognostic variables. This approach was extended for precipitation (Phillips et al. 2017b, 2020). Microphysical species are cloud liquid, cloud ice (or "crystals"), rain, snow, and graupel or hail. Prognostic variables were used to track ("tagging tracers") and estimate the mass and number concentrations of ice from each process of ice initiation (i.e., homogeneous freezing, primary and secondary) represented in the model. These variables are passive and do not interact with any other process in AC.

1) MODEL SETUP

The observed case of MCS has been simulated for a three-dimensional mesoscale domain of 40 × 40 grids with 2 km horizontal spacing with a time step of 10 s. A modeling study by Pauluis and Garner (2006) proved that in deep convective clouds, the statistics of vertical velocity and cloud properties (e.g., ice concentration) can be adequately represented with 2 km horizontal resolution.

TABLE 2. Two-day-averaged (9 and 12 May) observed aerosol mass mixing ratios from IMPROVE observations used as input to AC at levels of about 350–700 m MSL. However, all PBAP observations are from Amazonia (Patade et al. 2021).

Aerosol species	Mass mixing ratio (μg m^{-3})
Ammonium sulfate	0.7
Sea salt	0.061
Mineral dust	0.175
Black carbon	0.25
Soluble organic (80% of total organic)	1.38
Insoluble organic (20% of total organic)	0.345
PBAP (50% of insoluble organic carbon)	
Fungi	0.067
Bacteria	0.023
Pollen	0.053
Detritus	0.029
Algae	4.3×10^{-5}

The simulation time is 72 h, from 0000 UTC 10 May to 0000 UTC 13 May 2011. The vertical model resolution is about 0.5 km at all levels. The lateral boundary conditions are periodic in both the east–west and north–south directions of the domain and updated hourly, since the aim was to study MCS over several days, requiring an idealized "cloud-system resolving" model framework. An "idealized mode" simulation was performed by adding random humidity perturbations of about $\pm 8 \times 10^{-4}$ kg kg^{-1} in the PBL. The large-scale forcing of advective tendencies of heat and moisture were applied following Xie et al. (2014). These tendencies were updated hourly with continuous interpolation over time in between. The temperature and humidity fields were nudged toward the observation in the first 10 h of the simulation at the lowest model level in order to avoid an overshoot during the first peak of the simulation due to possible issues with the forcing [section 2a(2)] during the peak of the simulation.

Primary initiation of hydrometeors is governed by various aerosol particles (APs). These are ammonium sulfate, black carbon, sea salt, mineral dust, soluble and insoluble organics, and primary biological aerosol particles (PBAPs) group including, fungi, bacteria, detritus, pollen, and algae (Patade et al. 2021). AC predicts in-cloud aerosol size distribution (ASD) based on these APs (Table 2) and in-cloud supersaturation resolved on the model grid. The ASDs and resolved supersaturation are then input to the microphysics scheme to predict the number of cloud droplets and crystals nucleated (Phillips et al. 2017b).

Initial concentrations of APs are prescribed based on the Goddard Chemistry Aerosol Radiation and Transport (GOCART) model (Chin et al. 2000). Their vertical profiles were each rescaled by a constant factor to match with simultaneous measurements from the Interagency Monitoring of Protected Visual Environments (IMPROVE) at levels of stations (Ellis, Stilwell, and Wichita Mountains) near the simulated area. The present study used the IMPROVE aerosol mass

mixing ratios averaged for 9 and 12 May 2011. The rescaled initial mass mixing ratios of aerosol species are given in Table 2.

About 80% of the total organic carbon was assumed as soluble organic, and the remaining 20% was identified as insoluble organic carbon (Phillips et al. 2009). It was assumed that about 50% of insoluble organic aerosol particles were biological in origin. The contribution of these groups to the total PBAP mass is prescribed from the observations by Patade et al. (2021) over Amazonia (fungi: 39%; bacteria: 13%: pollen: 31%: detritus: 17%: algae: ~0.000 25%).

Droplets are activated both at cloud base (Ming et al. 2006) and by in-cloud droplet activation (Phillips et al. 2007, 2009). It depends on the size, number concentration, and chemistry of APs. AC predicts components of ASD of each APs that is immersed in (i) cloud particles and (ii) precipitation, and (iii) interstitial (Phillips et al. 2020).

The heterogeneous ice nucleation in AC takes place by APs such as mineral dust, black carbon, soluble organics, and PBAPs which predict INP activity from the "empirical parameterization" (EP) (Phillips et al. 2008, 2013). The EP represents all modes of INP activity such as contact freezing (outside-in and inside-out), deposition and immersion/condensation freezing, and heterogeneous raindrop freezing. Activation of ice crystals by these primary modes depend on temperature, supersaturation, and surface area mixing ratio for each APs.

There are two types of homogeneous freezing: cloud liquid/rain and solute aerosols (Phillips et al. 2007, 2009). Homogeneous freezing of cloud droplets near −36°C is treated by representing the preferential evaporation of smaller cloud droplets in the size distribution with a lookup table depending on the ascent and supersaturation in the mixed-phase updraft immediately below. This lookup table represents the fact that the larger cloud droplets freeze first homogeneously during ascent through the narrow temperature band of homogeneous freezing (e.g., PK97), with onset of supersaturation with respect to liquid causing the remainder to evaporate without freezing (Phillips et al. 2007).

2) Representation of SIP mechanisms in AC

Four types of SIP mechanisms are treated in AC. These are as follows:

1) The HM process of rime splintering

   The formation of secondary ice in the HM process depends on droplet size and temperature levels in the clouds (Hallett and Mossop 1974). Splinters of small ice particles are emitted during riming of supercooled cloud droplets (>24 μm) at levels between −3° and −8°C. The production rate of HM splinters is maximal at −5°C level. The HM process in AC is treated with a factor multiplying the fragment emission rate (350 splinters at −5°C mg^{-1} of rime) that depends on the mean cloud-droplet size (zero below 16 μm and unity above 24 μm, linearly interpolated in between).

2) Fragmentation in ice–ice collisions

   AC can generate secondary ice by fragmentation in ice–ice collisions. AC treats fragmentation in all types of ice particle collisions (Phillips et al. 2017a) with dependencies on temperature, ice morphology/size, and collision kinetic energy. The formulation of the fragmentation in ice–ice collisions is based on the principle of conservation of energy. Theoretically unknown parameters governing numbers of fragments emitted per collision are from field and laboratory studies by Vardiman (1978) and Takahashi et al. (1995). More details are from Phillips et al. (2017a, 2021).

3) Raindrop freezing fragmentation

   In AC, secondary ice formation due to raindrop/drizzle freezing is treated with an empirical formulation by Phillips et al. (2018). This formulation proposed two modes of raindrop freezing fragmentation based on previous laboratory observations (Phillips et al. 2018, references therein):

   (i) Fragmentation during freezing of spherical drop of drizzle or rain (mode 1): In this type, the quasi-spherical freezing may be initiated on collision of a supercooled drop (0.05–5 mm diameter) with a less massive ice particle or by heterogeneous raindrop freezing (immersed INP). In this mode, the spherical symmetry of the drop remains intact after collision with less massive ice particles, and it generates ice splinters when the outer shell breaks away following freezing. Both tiny and big fragments are generated.

   (ii) Fragmentation during the collision between a supercooled raindrop and a more massive ice particle (mode 2): This mode involves the collision of a more massive ice particle and raindrop. In this type of nonspherical freezing, collision with an ice crystal can disrupt the spherical symmetry of the drop. Secondary splash drops are emitted, some of which later freeze, forming ice splinters (Phillips et al. 2018; James et al. 2021).

   Both modes depend on the sizes of colliding hydrometeors and temperature. Fragmentation during raindrop freezing can create a high (~10^3) IE ratio when abundant large drops are present in the clouds (Phillips et al. 2018). More details are from Phillips et al. (2018).

4) Fragmentation during sublimation of snow and graupel

   Another SIP mechanism empirically formulated in AC is fragmentation during sublimation of graupel and dendritic snow (Deshmukh et al. 2022). Fragmentation during sublimation depends on the initial size of the ice particle, ambient RH_i, and a ventilation factor depending on the fall speed (Deshmukh et al. 2022). A dedicated tagging tracer for dendritic snow was used to track the ice particles formed in the dendritic region (−12° to −17°C) by heterogeneous nucleation and other SIP processes. This is then input to the dendritic sublimation breakup formulation in AC. Deshmukh et al. (2022) give more details of the formulation.

3. Results from the control simulation

a. Model validation

The convective line observed on 11 May 2011 in MC3E (section 2a) has been simulated by AC (section 2b). Figure 5a show the CCN activity spectrum predicted by AC from the

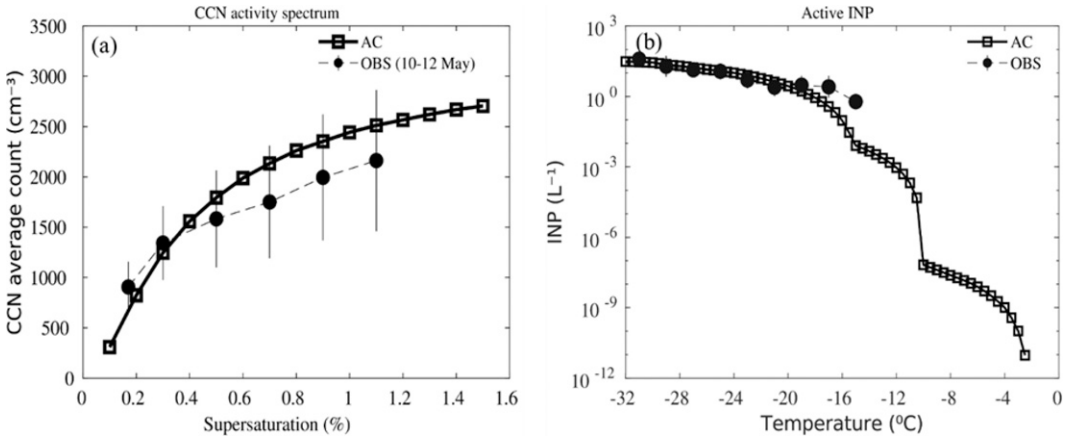

FIG. 5. (a) The CCN activity spectrum predicted by AC for the MC3E case (11 May 2011) for the environment at about 350 m MSL altitude, corresponding to the prescribed vertical profiles of size distributions of various species of aerosol (full line with squares). This is compared with the observed 3-day (9–12 May)-averaged CCN activity spectrum (dotted line with filled circles) from the CCN counter deployed at Lamont, Oklahoma. (b) The INP activity spectrum predicted by AC for 11 May 2011 MC3E case (full line with squares). This is compared with CFDC observation (dotted line with filled circles) taken at the SGP site in 2014 (adapted from DeMott et al. 2015, with changes). Standard deviations are plotted as a representative of error bars in (a) and (b).

prescribed ASD of soluble APs. It agrees with the observed CCN activity [section 2a(2)]. The MC3E campaign made no measurements of active INPs. However, DeMott et al. (2015) made continuous flow diffusion chamber (CFDC) measurements of active INPs in spring 2014 at SGP for a similar altitude. These data were reprocessed here for corrections and averaged over 2°C temperature bins for the same month as MC3E but for a different year (2014). Figure 5b shows that the number concentration of active INPs predicted by EP (AC) from the ASDs of insoluble aerosols (Table 2) is in good agreement with the observation.

Figures 6a and 6b show simulated domain averages of the accumulated surface precipitation and precipitation rate at the ground, respectively. The peaks in the simulated precipitation rate are at 2400 UTC 10 and 1900 UTC 11 May. However, observations show a maximum precipitation rate at 2000 UTC 11 May. The predicted precipitation rate is higher than that observed by about 30% in the first peak (2400 UTC 10 May) and about 40% less in the second peak of the simulation (1900 UTC 11 May). This may partly because of possible biases in large-scale forcing [section 2a(2)]. Also, it may reflect the classic overshoot for the onset of convection in cloud models generally. The initial period (1200–2400 UTC 10 May) involved predicted high CAPE (3500–4000 J kg^{-1}). More precipitation is observed in the second peak than in the first, despite the predicted lower CAPE (1700 J kg^{-1}) (1500–2100 UTC 11 May).

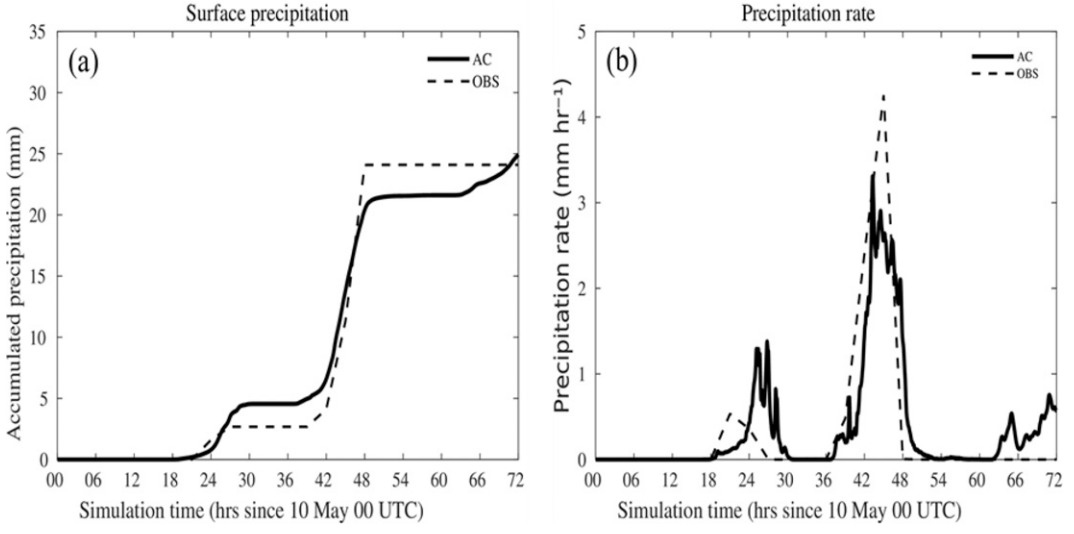

FIG. 6. Comparison of predicted (a) surface accumulation of precipitation and (b) surface precipitation rate from the control simulation with observations from rain gauge–adjusted WSR-88D over the SGP site.

For comparison, all predicted and observed cloud microphysical properties (Figs. 7 and 8) were averaged conditionally in an identical manner both for the same time period as the aircraft measurements (1600–2100 UTC 11 May 2011) and for regions of cloudy convective ascent, descent and of stratiform cloud. Since the Citation aircraft mostly flew in the stratiform region of the storm, a good agreement can be seen between the model and observations in the stratiform areas. For the simulation and aircraft observations, vertical velocities (w) exceeding 2 m s^{-1} were selected to identify convective updrafts, $w < -2$ m s^{-1} for downdrafts, and $|w| < 2$ m s^{-1} for stratiform conditions. The estimated errors in the vertical velocity from the aircraft observations are about ±30% from noise introduced by the aircraft maneuvers and the retrieval algorithms.

Considering the uncertainties involved in the measurements (as indicated by error bars), the predicted characteristics of cloud droplets such as droplet mean size, droplet concentration, and LWC are in fair agreement with the aircraft observations for cloudy convective ascent (Figs. 7a,d,h) and descent (Figs. 7c,f,j) as well as for stratiform regions (Figs. 7b,e,i). The observed LWC in the convective ascent below the freezing level appears much lower than in the simulation. This may reflect the tiny sample size (approximately a few seconds) of observational data points and lack of comprehensive sampling by the aircraft of cells at those low levels.

In cloudy convective updrafts, downdrafts, and stratiform conditions, the predicted NI_{200} (ice concentrations of particles > 200 μm) is about 10 L^{-1} at observational levels, the same order of magnitude as the aircraft data (Figs. 8a–c). The predicted NI_{200} in such regions has contributions from particles such as cloud ice (about 44%), graupel (about 32%), and snow (about 23%) with a minimal contribution from supercooled rain (<0.007%) in cloudy convective updrafts.

Supercooled cloud droplets in mixed-phase clouds will evaporate away if the supersaturation with respect to liquid water (s_w) becomes appreciably negative. Once the supercooled cloud liquid has evaporated, a deep mixed-phase cloud becomes ice-only, and there is cessation of vapor growth, riming, and production of ice precipitation, severing the positive feedbacks of ice multiplication (Yano and Phillips 2011). Evidence for precipitation being somehow necessary for any ice multiplication is that thin cold clouds without precipitation are observed by aircraft to have little difference between coincident concentrations of environmental INPs and total ice (Eidhammer et al. 2010).

At the onset of evaporation of liquid, $s_w = 0$, the theoretical critical ice particle concentration for this onset of subsaturation in the simulated storm is estimated following Korolev and Mazin [2003, Eq. (22) therein] in convective ascent. The predicted total ice concentration (Fig. 8a) is less than about a factor of 2 at warmer subzero temperatures (−5° to −25°C) from this coincident theoretical critical ice concentration, identically averaged conditionally in the convective ascent ($w > 2$ m s^{-1}). Comparatively, the agreement between these two parameters (theoretical and predicted ice concentrations) is much better at colder temperatures (<−25°C), because during mixed-phase ascent from the freezing level it takes time for the explosive ice multiplication to occur.

Moreover, the predicted actual number concentrations of ice particles greater than 1 mm, conditionally averaged over fast updrafts ($w > 2$ m s^{-1}) (Fig. 8d) and downdrafts ($w < -2$ m s^{-1}) (Fig. 8f) differs no more than 40% from the observations. In stratiform conditions ($|w| < 2$ m s^{-1}) the observed particle number concentration is about 70% higher than the predicted concentration at temperatures between −11° and −26°C (Fig. 8e).

Predicted domainwide averages of net shortwave (SW) and longwave (LW) radiative fluxes measured at the TOA agree with satellite observations. Errors at any given time are less than 25% (Figs. 9a,b). The simulated distribution of updraft speeds (>2 m s^{-1}) differs by no more than 50% from the aircraft observations (Fig. 9c). The predicted radar reflectivity agrees with the observations (KAZR) with a difference of less than about 5 dBZ at most subzero levels (Fig. 9d). A time–height plot of the radar reflectivity from AC is shown in Fig. 9e to compare it with the KAZR radar. The maximum predicted radar reflectivity is 40 dBZ at lower levels around 2000 UTC 11 May. The observed reflectivity was maximum (36 dBZ) around 1800 UTC. It can be seen that the simulated cloud tops were reached up to about 14 km (Fig. 9e), and the observed cloud tops up to about 12 km (Fig. 9f) MSL around 2000 UTC.

b. *Other analysis of control simulation*

Passive tagging tracers (section 2b) were added to track the various sources of ice from homogeneous nucleation, primary, and secondary processes represented in AC [section 2b(2)]. From their vertical profiles in Figs. 10d–i, it can be seen that fragmentation in ice–ice collisions is the most prolific (~80%) at all subzero levels among all four SIP mechanisms in convective updraft, downdraft, and stratiform conditions and creates IE ratios as high as 10^3 (Figs. 10j–l), when considered over the duration of the simulation.

As the simulated MC3E case had relatively warm cloud bases (~17°C), the HM process is active at temperatures between −3° and −10°C in updrafts (Fig. 10d), creating IE ratios ~10^3 (Fig. 10j) at these temperatures. In downdrafts, fragmentation during sublimation is the second most prolific (~20%) SIP mechanism and creating IE ratios of up to about 10^2 (Fig. 10k). As the simulated MC3E case had relatively low mean droplet diameters (<18 μm, Fig. 7a) at levels colder than 0°C, there is less coalescence than the cold-rain process (Fig. 15 below), and raindrop freezing fragmentation (Figs. 10d–i) contributes less (<1%) than the cold-rain process to the SIP and creates less IE ratio (~10). It is also predicted that throughout the vertical levels in clouds, fragmentation in ice–ice collisions creates IE ratios on the order of 10^3 in convective cloudy updrafts, downdrafts, and stratiform conditions.

Figures 11a and 11b show the time series of predicted ice concentrations conditionally averaged over all cloudy vertical levels throughout the domain, and IE ratios in the first hour after the onset of the convection. At times less than 10 min after the onset of ice, the HM process dominates the overall

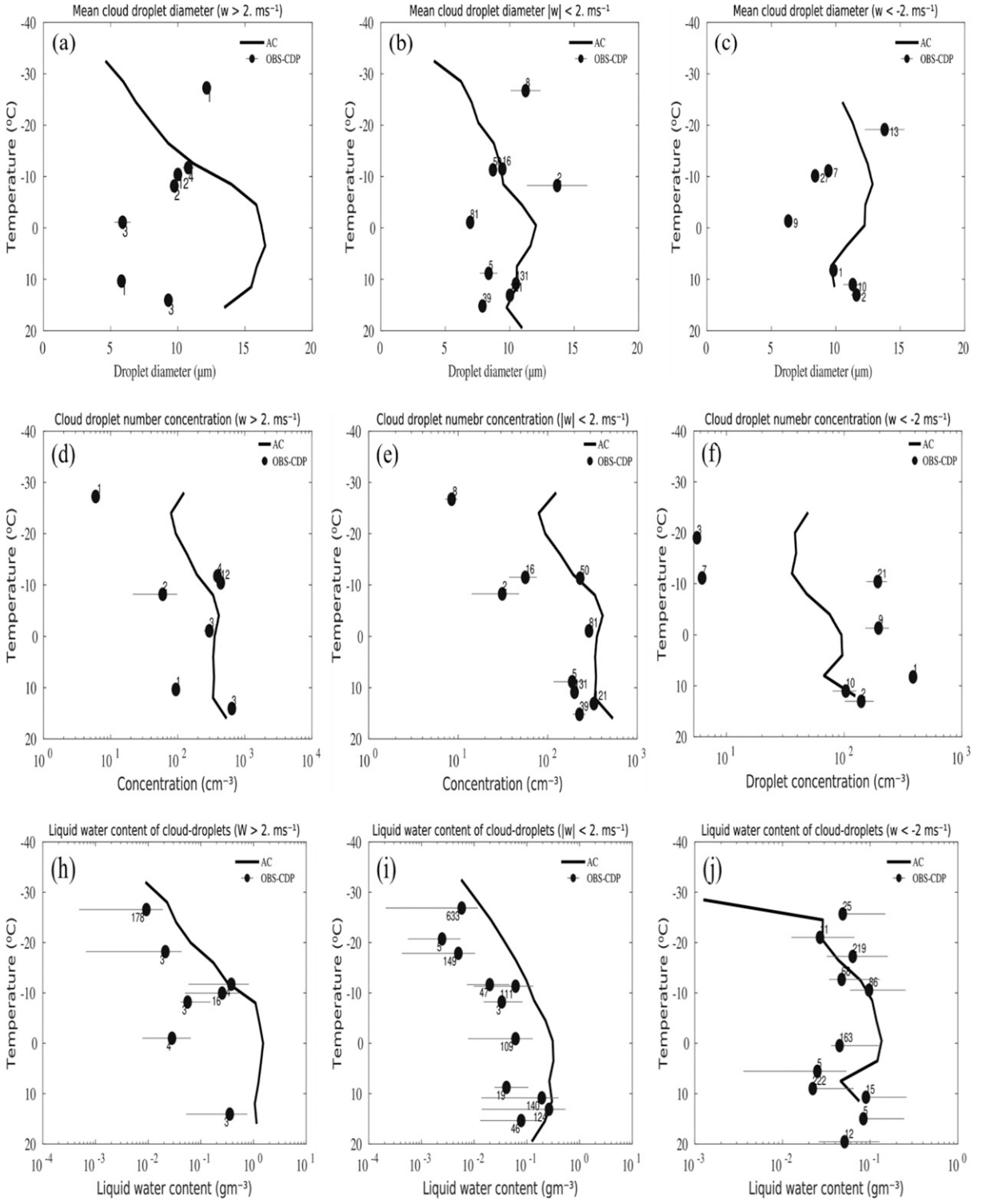

FIG. 7. Predicted (a)–(c) mean cloud droplet diameter and (d)–(f) droplet number concentrations compared with observations from the CDP probe and (g)–(i) liquid water content from the control simulation conditionally averaged over cloudy convective updrafts ($w > 2$ m s^{-1}), stratiform ($|w| < 2$ m s^{-1}) and downdrafts ($w < -2$ m s^{-1}) conditions compared with the aircraft observations from the CDP probe. Error bars shown in (a)–(i) are standard errors of observational samples. Numbers above each observation data point show the time (in s) for which the aircraft sampled the cloud at that level. Note that each observational data point consists of typically multiple up- and downdraft sampled for the convection.

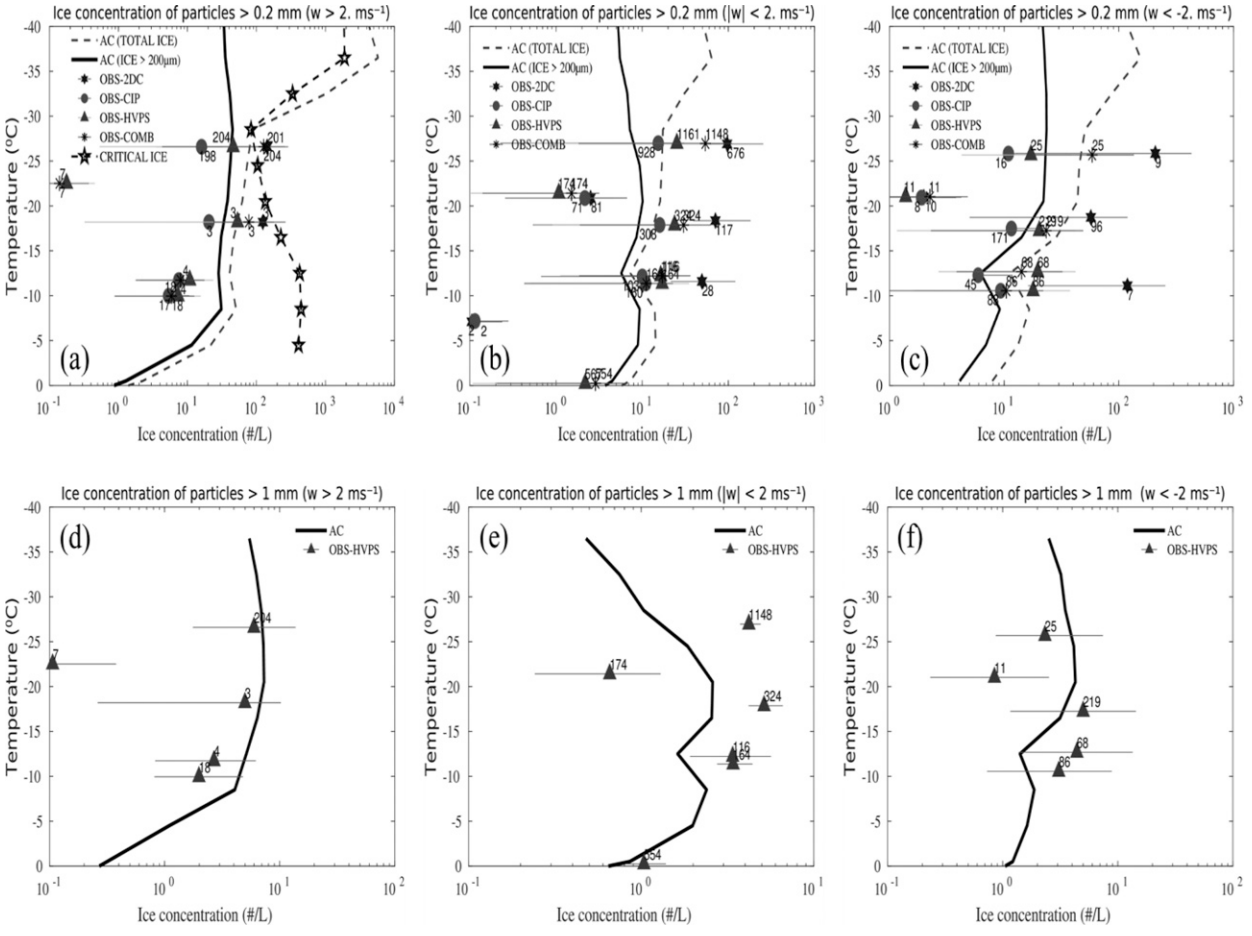

FIG. 8. Comparison of predicted ice number concentrations for particles of maximum dimension > 0.2 mm of all microphysical species (cloud ice, snow, and graupel/hail) (full black lines) over cloudy convective (a) updraft ($w > 2$ m s^{-1}), (b) stratiform ($|w| < 2$ m s^{-1}), and (c) downdraft ($w < -2$ m s^{-1}) regions with aircraft observations from the 2DC, CIP, HVPS-3 probes, and combined spectrum (COMB) of these three probes. Also shown in (a) is the theoretical critical concentration of ice particles (pentagrams) calculated from Korolev and Mazin [2003, Eq. (22) therein], conditionally averaged similarly for convective ascent. (d)–(f) Number concentrations of all ice particles bigger than 1 mm in such updrafts, stratiform, and downdrafts conditions compared with aircraft observations from the HVPS-3 probe. Error bars shown are standard errors of observational samples. The total duration (seconds) for which the aircraft sampled the cloud at any particular level is displayed with numbers on each observational data point.

ice concentration, causing an exponential growth of crystal numbers. Immediately in the first 10 min, it creates average IE ratios as high as 10^2 (Fig. 11b). As the clouds grow further with time and tops ascend through the mixed-phase region, the exponential growth is continued by fragmentation in ice–ice collisions, which becomes the most prolific SIP mechanism after 10 min as snow and larger graupel particles increase in concentration (Fig. 11c). The concentrations of activated INPs, from the tagging tracers required for the EP (as cloud top ascends), and total ice increase together, sustaining IE ratios $\sim 10^4$. The ice concentration attains its maximum after the first half hour, becoming quasi steady for the rest of the lifetime of the MCS. These quasi-steady ice concentrations are accompanied by declining IE ratios after the first half hour with a minimum (about 10^2) toward the end of the simulated MCS.

The dependency on the vertical velocity of predicted IE ratios conditionally averaged over the entire domain between 0° and −30°C is shown in Fig. 12b. The total IE ratios have the same order of magnitude in the updraft and downdraft (>-5 m s^{-1}) regions, whereas in the stratiform region, the IE ratio is minimal (about 40). The balance among various SIP mechanisms in convection differs between ascent and descent (Fig. 12a). The SIP mechanism of fragmentation in ice–ice collisions dominates overall ice concentrations in convective ascent and descent, throughout the simulation. However, in most convective downdrafts, fragmentation during sublimation of ice is the second most prevalent process of SIP, creating IE ratios as high as 10^2 in the fastest downdrafts (<5 m s^{-1}). Generally, the faster the ascent or descent in all simulated cold clouds, the greater the IE ratio.

Figures 13a and 13b show a number budget of ice particles initiated by all processes represented throughout the control simulation. Fragmentation in ice–ice collisions generates 100 times more particles than heterogeneous ice nucleation at all

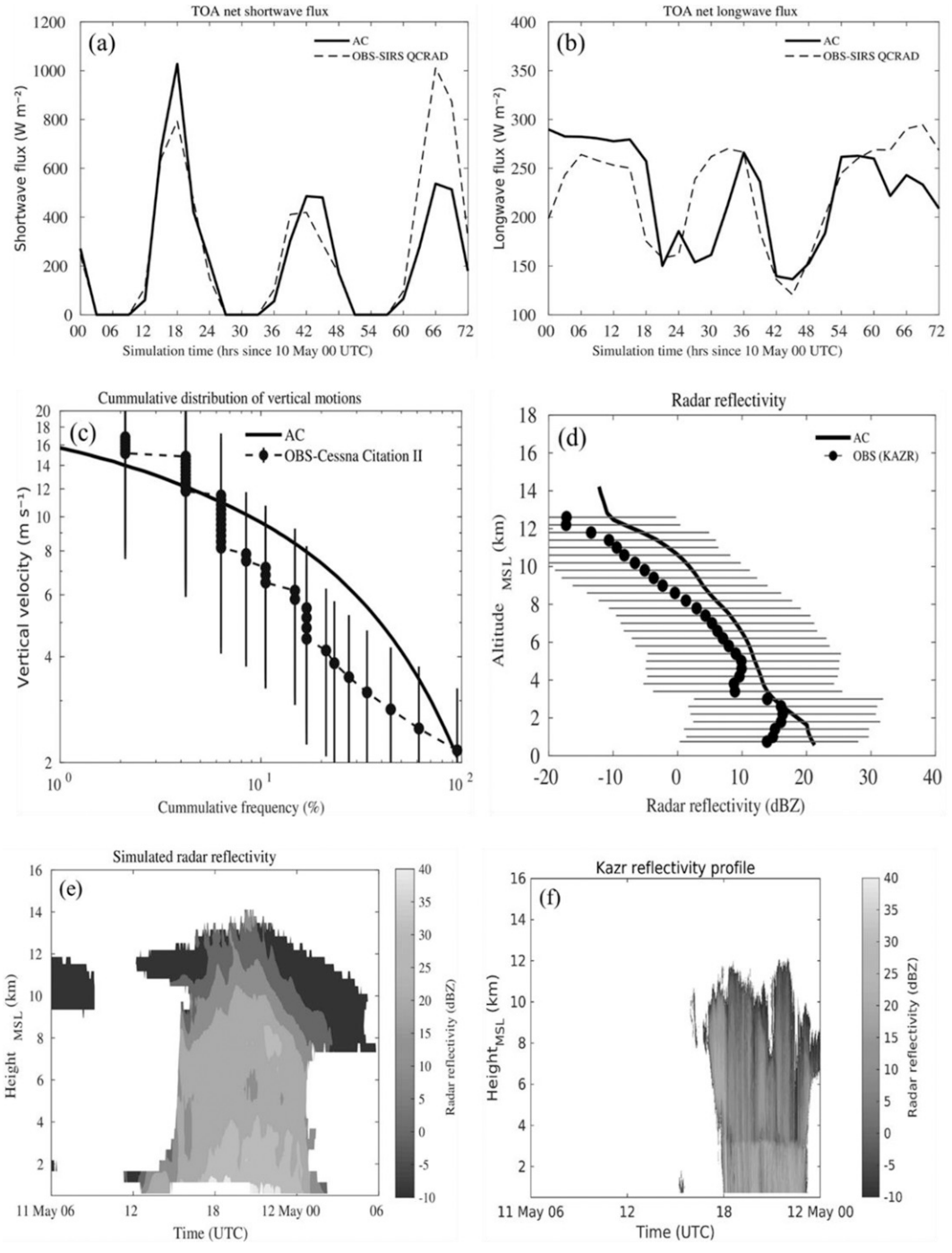

FIG. 9. Comparison of predicted (a),(b) TOA net shortwave and longwave radiation flux compared with that from GOES-VISST data, (c) vertical velocity histogram in fast convective updrafts (>2 m s^{-1}) compared with observations from the Citation aircraft, and (d) the simulated and observed vertical profiles of radar reflectivity conditionally averaged over the regions of significant reflectivity (>-10 dBZ) at each level, from the ground-based (KAZR) radar, which was functional at CF, Lamont, Oklahoma (36.605°N, 97.485°W). Error bars in (c) and (d) are standard errors of observational samples. Comparison of (e) simulated radar reflectivity profile with (f) reflectivity observed by KAZR.

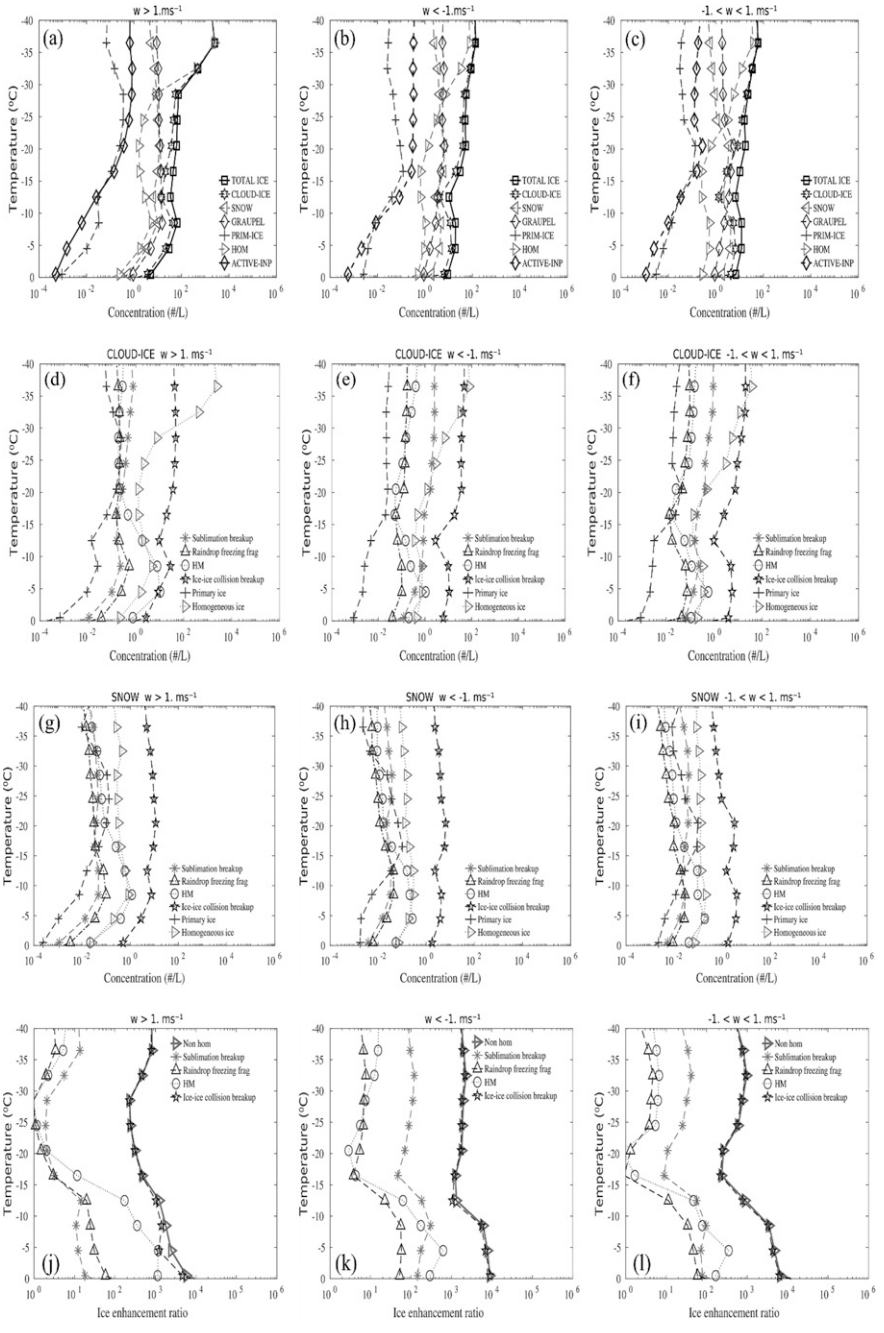

FIG. 10. Number concentrations for different microphysical species and various tracer terms defining SIP processes in the control simulation of AC, conditionally averaged over regions of cloudy convective (left) updrafts (>1 m s^{-1}) and (center) downdrafts (<−1 m s^{-1}) and (right) stratiform cloud ($-1 < w < 1$ m s^{-1}). Properties displayed for these three regions are (a)–(c) number concentrations of activated INPs (solid line with diamonds), ice number concentrations (L^{-1}) of all particles (solid line with squares) and individual microphysical species; cloud ice, snow, and graupel (dotted lines with hexagons, downward-pointing triangles, diamonds, respectively), (d)–(f) concentration of cloud ice from the tagging tracers of fragmentation during sublimation breakup (asterisks), shattering due to raindrop freezing (upward-pointing triangles), the HM process (open circles), and fragmentation in ice–ice collisions (pentagrams) averaged for (g)–(i) snow concentration from these tracer terms, and (j)–(l) IE ratios from nonhomogeneous ice and tracer terms of various SIP processes. Number concentrations of primary ice (plus signs) from heterogeneous ice nucleation and homogeneous ice (right-pointing triangles) are shown in (d)–(i).

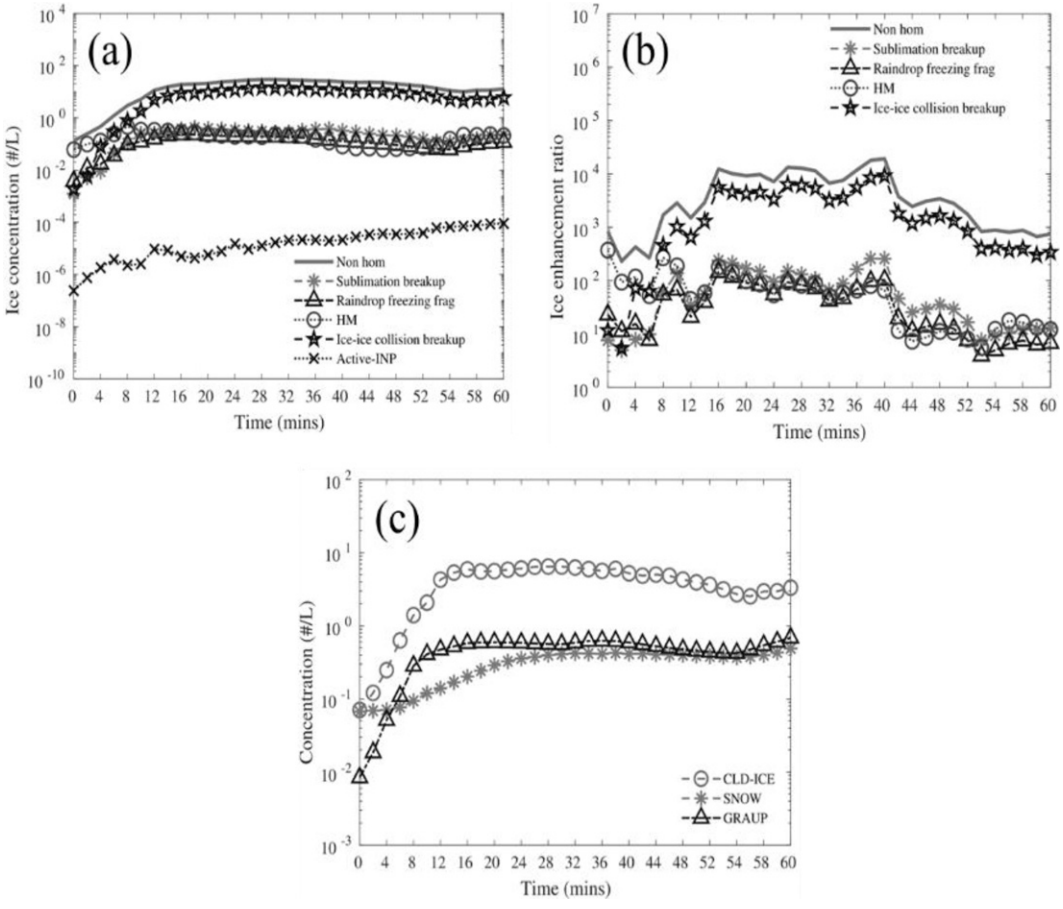

FIG. 11. The number concentration of ice particles (a) for total nonhomogeneous ice (total ice from cloud ice and snow minus total homogeneously nucleated ice) (solid line) and various tracer terms defining SIP processes such as the HM process (open circles) and fragmentation during sublimation (asterisks), raindrop freezing (upward-pointing triangles) and ice–ice collisions (pentagrams) and activated INP (crosses) in the control simulation of AC, (b) IE ratio defined from (a) for nonhomogeneous ice and ice from various tagging tracers used to track SIP processes and (c) concentration of cloud ice (open circles), snow (asterisks), and graupel (upward-pointing triangles). All concentrations in (a)–(c) are conditionally averaged between temperatures 0° and −30°C for nonzero values. The plotted time is relative to the second onset of the convection at 1400 UTC 11 May 2011.

temperatures warmer than −30°C. Among all types of fragmentation in ice–ice collisions, fragmentation due to collisions of snow with graupel or hail is the most prolific (~44% of all fragments from all ice–ice collisions, Fig. 13c). Also, collisions of graupel with either graupel or hail (~10% fragments from all ice–ice collision) and collisions of snow on snow are predicted to have appreciable impacts on the budget (~27% of fragments from fragmentation in ice–ice collisions, Fig. 13c).

At first glance, the budget gives the impression that the fragmentation during sublimation of graupel is the most prolific SIP mechanism as it generated about 400 times more ice particles than the heterogeneous ice nucleation at temperatures warmer than −30°C. However, as noted above (section 3b, Fig. 10), the tagging tracers reveal that the fragmentation during sublimation of ice is less prolific than the HM process and fragmentation in ice–ice collisions. A separate budget (Fig. 13a, black bar) shows that the vast majority (~80%) of such fragments from fragmentation during sublimation are sublimated away completely while descending, so never reach the updrafts for growth and survival, and only about 20% of these emitted fragments survive (Fig. 13a, yellow bar).

Figure 13a also shows that homogeneous freezing produces most ice particles (~94% of the total budget) in the entire storm as clouds reach above the −36°C level. This is much greater than the total ice formed in all SIP processes (~3% of all ice initiated). Primary ice crystals formed at warmer temperatures (>−30°C) contribute only about 0.05% to the total ice formed.

Figure 14 shows the dependency of the total number of ice particles initiated in the simulated storm from the HM process and fragmentation in ice–ice collisions on vertical velocity and temperature. Most of the splinters from the HM process (~80%) were emitted between temperatures −5° and −8°C and weak convective ascent vertical velocities between 1 and

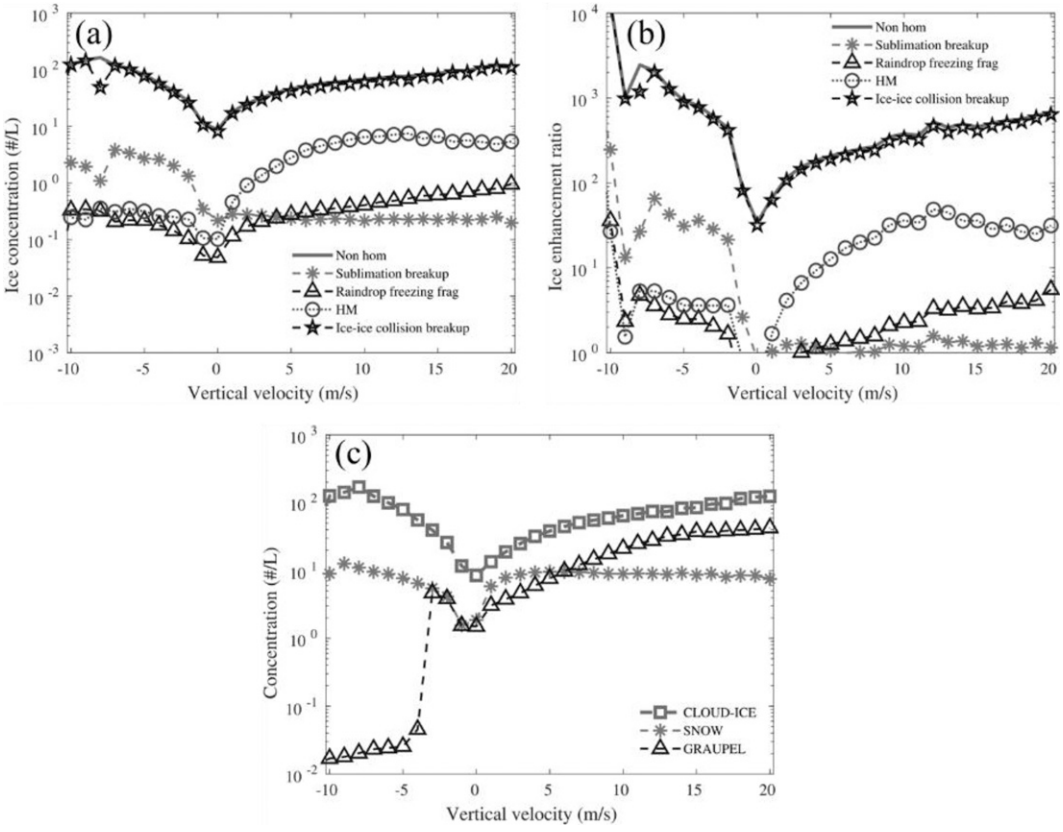

FIG. 12. Domain-averaged distributions with respect to the ascent of (a) the predicted nonhomogeneous ice (total ice from cloud ice and snow minus total homogeneously nucleated ice) (solid line) and ice (cloud ice + snow) from tagging tracers of various SIP processes such as the HM process (open circles) and fragmentation during sublimation (asterisks), raindrop freezing (upward-pointing triangles), and ice–ice collisions (pentagrams) averaged for vertical velocities between −10 and 20 m s^{-1} over 1 m s^{-1} bin at temperatures between 0° and −30°C. (b) IE ratios at these vertical velocity bins were estimated from (a),(c) concentrations of cloud ice (squares), snow (asterisks), and graupel (upward-pointing triangles).

5 m s^{-1} (Fig. 14a). About 20% of all HM ice splinters were generated in stronger updrafts (>5 m s^{-1}) at those temperatures. Fragmentation in ice–ice collisions generated about two orders of magnitude more ice particles than the HM process (Fig. 14a) in the entire simulation and is the most prolific mechanism of SIP overall. Fragmentation in ice–ice collisions mostly happens in convective ascent greater than 1 m s^{-1} (~70%) and temperatures in the central third of the mixed-phase region (−15° to −30°C). In a faster convective ascent, emission of fragments occurs at colder temperatures (Fig. 14b), as expected from graupel and snow being upwelled to higher levels. In the stratiform clouds, the peak in fragmentation in ice–ice collisions is in the lower third of the mixed-phase region (0° to −10°C).

Figure 14b illustrates how fragmentation in ice–ice collisions is ubiquitous throughout the storm. This budget of fragments initiated is consistent with the vertical profiles noted above, showing fragments from fragmentation in ice–ice collisions at all subzero temperatures (Fig. 10a). Fragmentation in ice–ice collisions is more evenly distributed over temperatures (Fig. 14d) than the HM process. It has a broad thermal peak in the central mixed-phase region (near −20°C) due to an interplay between supercooled cloud liquid for riming and the fallout of graupel during upwelling. About 70% of the fragments are generated in the upper half (−20° to −36°C) of the mixed-phase region due to the upwelling of both large graupel and snow particles (Fig. 10a). Most of the fragments (about 65%) from fragmentation in ice–ice collisions are emitted in weak to moderate convective ascent (<10 m s^{-1}) (Fig. 14c), partly because the weaker ascent is more ubiquitous. By contrast, raindrop freezing fragmentation and the HM process contribute only about 1% of all fragments from all four SIP mechanisms (Figs. 13a,b).

Figure 15 shows the components of graupel from the two precipitation mechanisms (section 1), namely, the warm rain and ice-crystal processes ("warm" and "cold" graupel, respectively), diagnosed with passive tagging tracers. The lack of warm rain causes a lack of raindrop freezing, and hence cold graupel is more prolific than warm graupel. This can be attributed to typically high CCN concentrations (>2000 cm^{-3}, Fig. 5a) suppressing coalescence and related raindrop freezing. The continental aerosol conditions act to boost the mass

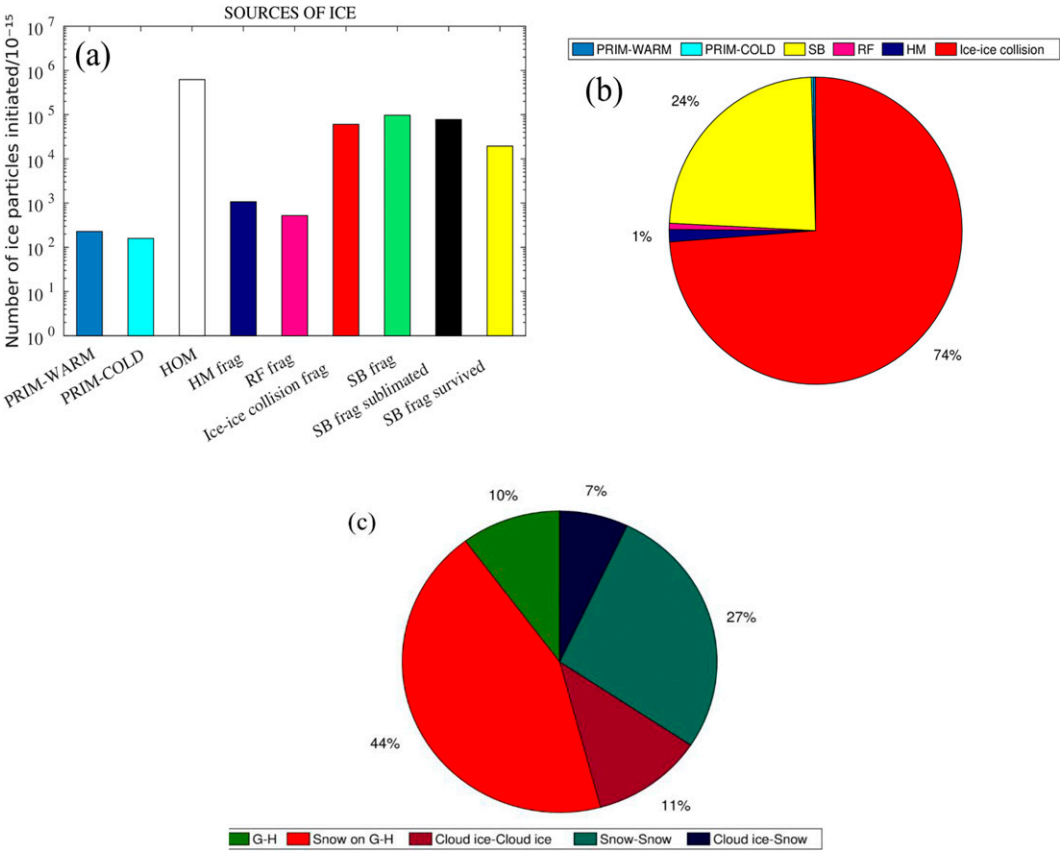

FIG. 13. (a) Bar chart for budgets of the number of ice crystals from homogeneous, primary, and secondary initiation in the control simulation of the AC for 11 May 2011 MC3E case. From left to right, bars are the sources of heterogeneous ice nucleation at temperatures warmer ("PRIM-WARM") and colder ("PRIM-COLD") than −30°C, homogeneous freezing at temperatures colder than −36°C ("HOM"), and various SIP mechanisms. These are the HM process of rime splintering ("HM frag"), fragmentation of freezing rain/drizzle ("RF frag"), fragmentation in ice–ice collision (ice–ice collision frag) from all types of collision, fragmentation during sublimation of dendritic snow and graupel (SB frag). The number of sublimationally generated fragments (SB frag) that are sublimated away is also shown ("SB frag sublimated"). Still, only a few of them can reach the updrafts and survive since most of them must melt in the downdrafts ("SB frag survived"). (b) the same information, but in a pie chart without including homogeneously nucleated ice. (c) Another pie chart shows the relative contributions of various types of fragmentation in ice–ice collisions including collisions of graupel with either graupel or hail (G–H), snow on graupel or hail (Snow on G–H), ice crystal on ice crystal (Cloud ice–Cloud ice), snow on snow (Snow–Snow) and crystal on snow (Cloud ice–Snow).

of supercooled cloud liquid available for riming (Saleeby et al. 2016; Braga et al. 2017) yet may also decrease the graupel–drop collision kernel (Cui et al. 2011). However, raindrop freezing is not insignificant in the MC3E control run and can accelerate any SIP process. Collisions between ice crystals and trace amounts of supercooled warm rain can reduce the onset time of both the HM process and fragmentation in ice–ice collisions (e.g., Phillips et al. 2001; Yano and Phillips 2011).

c. *Cloud-top dependency of SIP*

Airborne measurements by H80 in Miles City, Montana, sampled developing cumulus clouds at levels warmer (by between 2 and 17 K) than the instantaneous cloud tops. To estimate the IE ratio, H80 used the PBL measurements of active INPs and the temperature of activation was assumed to be cloud-top temperature. This yielded the classic plot of IE ratio as the function of cloud-top temperature (Fig. 1) with peaks at characteristic temperatures (e.g., ~−12°C).

Consequently, to analyze the causes of that classic plot, we have inferred a similar relation from the control simulation, partly using tagging tracers noted above (section 2b). In the present study, the simulated clouds sampled were mostly young and convective (Fig. 16c) with ascending tops. The estimated average age of these clouds was typically between 5 and 30 min. Figure 16a shows predicted number concentrations of active INPs and ice particles derived from the cloud-top algorithm (appendix), plotted against temperatures of coincident cloud tops warmer than −30°C. Only cloud tops below the −36°C level were chosen to exclude all ice from homogeneous freezing. Tagging tracers of cloud ice and

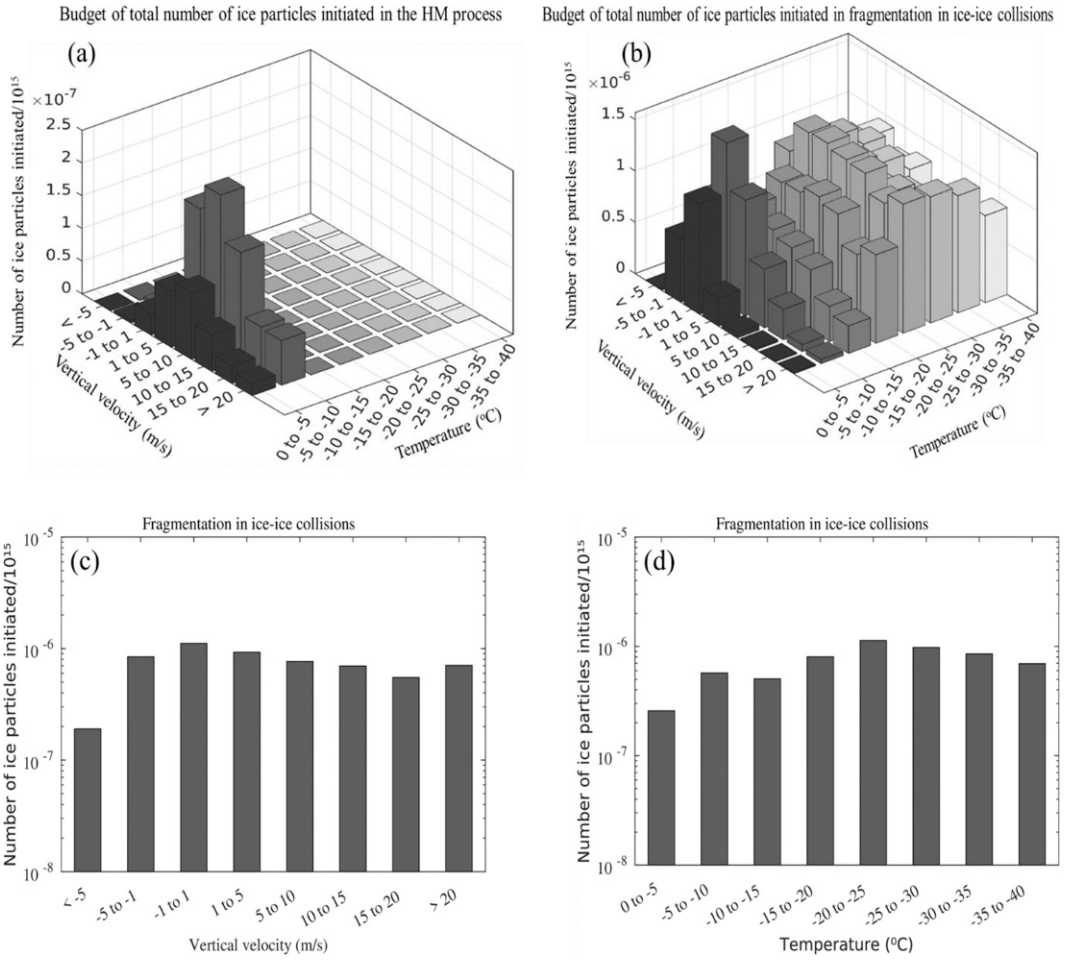

FIG. 14. Budget of the total number of ice particles initiated in the (a) HM process and (b) ice–ice collisions in ranges of vertical velocity (m s^{-1}) and temperature (°C) for the entire simulation. (c),(d) The same information is shown for fragmentation in ice–ice collisions.

snow from homogeneous freezing were deducted from the predicted total concentrations of cloud ice and snow to ensure no homogeneous ice in the IE ratio analysis at levels warmer than −36°C. From the simulation output, coincident values of concentrations of active INPs (prognostic scalars from the EP) and ice particles were taken from the nearest level (up to 7 K warmer) below the cloud top, where both were nonzero. Figure 16b shows the profile of the IE ratio derived from Fig. 16a. It can be seen that the IE ratios (Fig. 16b) generally tend to decrease with decreasing temperature of cloud top, as seen by H80 (Fig. 1, section 1).

Moreover, the predicted and observed (H80, Fig. 25 therein) IE ratios show a peak at similar cloud-top temperatures (~−12°C). This peak chiefly arises from the HM process but partly also from fragmentation during ice–ice collisions and raindrop freezing (Fig. 16b). However, the contribution to the IE ratio is predicted to be strongly dependent on vertical velocity. For example, with vertical velocity > 1 m s^{-1} (not shown here), the peak (~10^3) in IE ratio is mainly from the HM process and fragmentation in ice–ice collisions. However, at higher updraft speeds ($w > 5$ m s^{-1}, not shown here), the raindrop freezing fragmentation becomes the second most prolific SIP mechanism after the HM process. It is predicted that the splinters from the HM process tend to accumulate near the −12°C level due to increased stability of the atmosphere above this level (Fig. 17). While any typical cloud is growing (e.g., as cumulus congestus) toward the mature stage, fragmentation in ice–ice collisions becomes the most prolific SIP mechanism after the cloud top ascends above the −20°C level, as mentioned below (section 5).

This explanation for the observed peak in IE ratio is consistent with previous aircraft studies (Hallett et al. 1978; Harris-Hobbs and Cooper 1987; Blyth and Latham 1993). Such studies suggested that the HM process is the dominant SIP mechanism in convection. Inspection of such studies shows that they tended to sample in young, developing cumulus clouds, typically less than about 15 min after the ascending cloud top first goes above the freezing level, and with warm bases such that large cloud droplets (>24 μm) are present in the HM generation region (−3° to −8°C).

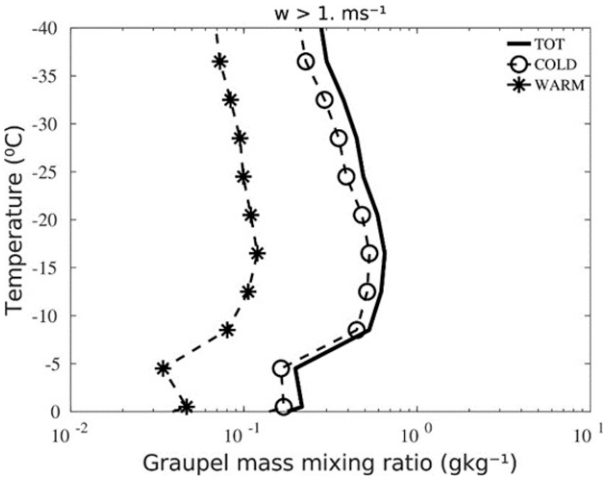

FIG. 15. Domain-averaged profile of mass mixing ratio of total graupel (solid line), cold graupel (open circles), and warm graupel (asterisks) conditionally averaged over cloudy convective updrafts ($w > 1$ m s^{-1}).

The HM process is predicted to prevail in the overall SIP for ascending cloud tops between the −7° and −12°C levels and creates IE ratios as high as 10^3 in such young growing convective clouds (Fig. 16b). This situation for convective cells in their growth stage contrasts with the vertical profiles averaged for the entire simulation (Figs. 10d,g), during which the mature stage dominates over long times. Essentially, the HM process is faster than fragmentation in the ice–ice collisions and can prevail in younger clouds with warmer cloud tops (Fig. 13a). The HM process is proportional to the total riming rate of graupel. In contrast, fragmentation in ice–ice collisions is slower yet eventually more powerful, with its positive feedback between riming of snow to become graupel, snow–graupel collisions, and growth of fragments to become snow (Yano and Phillips 2011, their Fig. 4; Phillips et al. 2017b). This difference in natural time scales of the explosive growth of ice concentrations among these SIP mechanisms explains why studies by aircraft of warm-topped (warmer than −36°C) ascending turrets have frequently reported strong correlations of observed ice concentrations with the HM process (Hallett et al. 1978; Harris-Hobbs and Cooper 1987; Blyth and Latham 1993; Blyth et al. 1997; Huang et al. 2017; Gayatri et al. 2022; Lasher-Trapp et al. 2021) as noted above. Such warm-topped turrets tend to be young. For example, in the present simulation, a turret with a top ascending through the −20°C level and a peak updraft speed of about 10 m s^{-1} has spent typically only about 10 min above the freezing level.

A wide range of intensities of various SIP mechanisms is evident in cloud-top spectrum of ice concentrations shown in Fig. 16a. The peak from the HM process noted above consists of IE ratios as high as 10^3 at −7° to −12°C in the lower half of the mixed-phase region. Fragmentation during ice–ice collisions and raindrop freezing are each jointly the second most prolific SIP mechanism for ascending cloud tops near −12°C with IE ratios ~ 10^2. Later as cloud tops ascend toward the upper half of the mixed-phase region, going above the −15°C level, the explosive growth of ice crystal concentrations is mainly from the fragmentation in ice–ice collisions and contributes more than 90% to the total ice formed in all SIP processes (Fig. 16a), sustaining IE ratios ~10^2 at these temperatures (<−15°C). This is consistent with laboratory observations by Vardiman (1978) and Takahashi et al. (1995) for fragmentation in ice–ice collisions, showing a strong dependency on temperature with a maximum rate of splinter ejection at about −15°C for dendritic cloud ice and snow. Moreover, fragmentation during raindrop freezing and sublimation can be ranked as the third and fourth most prolific SIP mechanisms, respectively, creating IE ratios of about ~10^2 and 10, at temperatures between −7° and −15°C.

H80 used the PBL measurements of active INP and assumed that the activation temperature is simply the instantaneous cloud-top temperature. Although elsewhere in the present study a more accurate estimate of active INP is followed, for the sake of comparison with H80, their approach is now followed in Fig. 18a. Predicted active INP concentrations were obtained from the PBL during convection, and the temperature of activation was assumed to be the cloud-top temperature. Corresponding predicted IE ratios for cloudy convective updrafts (>2 m s^{-1}) are shown in Fig. 18b. IE ratios predicted and observed by H80 are on the same order of magnitude, as differences are comparable to errors in the IE ratio observed by H80. From Fig. 18b, it can be seen that the peak in the IE ratio (10^3) observed by them is due mainly to the HM process, if it is assumed that the warm-based continental deep convection of our MC3E case resembles that observed by H80.

4. Results from sensitivity tests

Various sensitivity tests (Table 3) were performed to evaluate the role of different SIP mechanisms for the IE ratio. This involved modifying the control run to create various perturbation simulations, which were then compared with the control run.

Figures 19a and 19b show the cloud-top dependency of ice concentration and IE ratios for various tests. In the absence of either the HM process or fragmentation in ice–ice collisions, the IE ratio decreases by a factor of about 20 compared to the control simulation in the middle and upper half of the mixed-phase region (Fig. 19b). In the case of no fragmentation in ice–ice collisions, IE ratios in the upper half of the mixed-phase region decrease sharply with minimum 1° at −23°C cloud-top temperature. However, only a factor of about 2 change is seen in the IE ratios in the case of "no raindrop freezing fragmentation" case and "no fragmentation in sublimation" case at cloud-top temperatures near −10°C (Fig. 19b).

Ice concentrations are plotted against cloud-top temperatures for various sensitivity tests (Figs. 19c–f). It can be seen that the HM process is the dominant SIP mechanism at cloud-top temperatures warmer than −12°C contributing ~80% to the total nonhomogeneous ice from all four SIP processes at these temperatures in "no fragmentation in ice–ice collisions" case, "no raindrop freezing fragmentation" case, and "no fragmentation

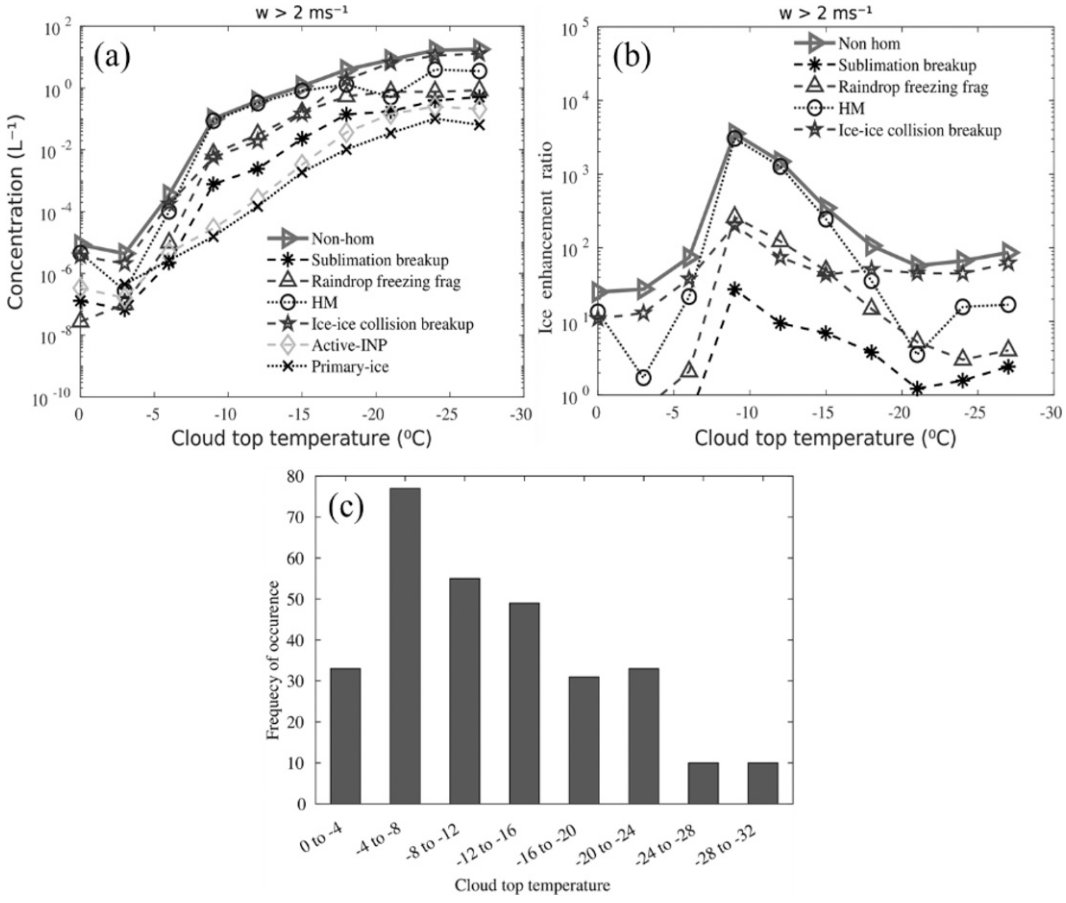

FIG. 16. (a) Predicted concentration of active INP (diamonds) from the EP, heterogeneously nucleated ice (crosses), total nonhomogeneous ice (total ice from cloud ice and snow minus total homogeneous ice) (right-pointing triangles) as a function of cloud-top temperatures conditionally averaged over cloudy convective updrafts (>2 m s^{-1}), ice concentration tracked by tracers (cloud ice + snow) from sublimation breakup of dendritic snow and graupel (asterisks), fragmentation during raindrop freezing (upward-pointing triangles), the Hallett–Mossop (open circles), and fragmentation in ice–ice collisions (pentagrams). Concentrations of active INP and total ice from control and individual SIP mechanism are at temperatures warmer (1°–7°C) than the cloud top. All the concentrations are the geometric means of nonzero values. (b) Predicted IE ratio as a function of cloud-top temperatures for cloudy convective updrafts (>2 m s^{-1}) of clouds sampled by the cloud-top algorithm for the simulated MC3E case, and (c) frequency of occurrence of cloud tops at various temperature ranges.

during sublimation" case (Figs. 19d–f). Fragmentation in ice–ice collisions is the most prolific, contributing over 70% to the total nonhomogeneous ice formed in all SIP processes at all cloud-top temperatures in the absence of the HM process (Fig. 19c). When present in young cumulus clouds whose tops are growing, the fragmentation in ice–ice collisions contributes < 30% to the total nonhomogeneous ice at cloud-top temperatures between 0° and −15°C. The HM process contributes over 50% to nonhomogeneous ice at cloud-top temperature ~ −7°C.

The radiative response of cloud depends on multiple factors such as cloud type and cover, hydrometeor concentrations and habits, liquid, and ice water path (Kinne and Liou 1989; Hong et al. 2016; Young et al. 2019). The enhanced ice due to SIP reduces the cloud cover and increases the SW flux reaching the climate system (Young et al. 2019). Figure 20 shows the TOA SW and LW for the control and various sensitivity test runs (Table 3). It reveals that clouds in which SIP or fragmentation in ice–ice collisions is not active show a significant drop in both net SW (by about 8%, Fig. 20a) and LW (by about 12%) radiative fluxes at the TOA (Fig. 20b). This change can be attributed to the increase in cloud cover and LWC (not shown here) at the middle and upper half of the mixed-phase region. The rapid glaciation ceases in the absence of these processes, increasing cloud cover and lifetime.

Schematic picture of multiple SIP processes

A schematic structure of growing cloud with cloud base ~ 15°C and cloud tops extending from −5° to −50°C from the control simulation is shown in Fig. 21a. It can be seen that in a typically young cloud with a top ~ −5°C, SIP processes are absent. As the cloud grows further, with its tops reaching

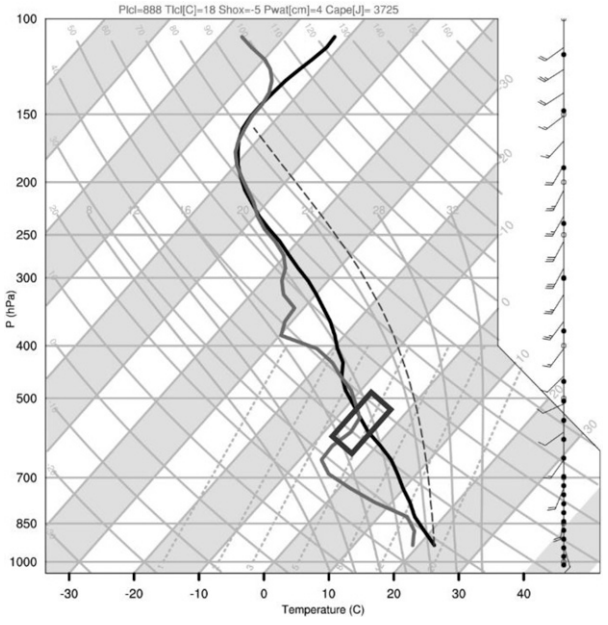

FIG. 17. The instantaneous profile of thermodynamic sounding plotted for the simulation in convection when the HM process was active showing stability at levels above the HM region (−3° to −8°C). The lines shown are environment temperature (black line), dewpoint temperature (gray line), and pseudoadiabat (dotted black line). The black box indicates the HM generation region.

up to −15°C level, the HM process is active (−3° to −8°C) and dominates (~96%, Fig. 21b) overall ice concentrations, even at levels up to the cloud top due to upwelling of the splinters formed below. Other SIP mechanisms such as the fragmentation in ice–ice collisions, raindrop freezing fragmentation, and fragmentation during sublimation are also present but contribute less (<2%) to the total ice than the HM process in clouds with relatively warm (~−15°C) tops. When the cloud becomes older with tops reaching above the −30°C level, these other SIP mechanisms become more active than they were before. The fragmentation in ice–ice collisions is the most prolific at all the temperatures throughout the cloud structure, contributing more than 90% to total ice at temperatures < −15°C. Second, fragmentation during sublimation and raindrop freezing are primarily active at temperatures colder than −10°C and contribute <2% to the total ice concentration. Homogeneous freezing is the dominant process of ice initiation as convection reaches above the −36°C level.

Figure 21b shows a pie chart corresponding to each cloud growing from cloud-top temperature −15° to −50°C. In the early developing stage, when the cloud grows from top ~ −5° to −15°C in 5–10 min, under the suitable condition, splinters can be produced by the HM process and is the dominant SIP mechanism in such clouds. When clouds grow further in 15–20 min, reaching up to level −30°C large-sized graupel number increases, and as a result, the fragmentation in ice–ice collisions becomes faster than the HM process. When a convective cloud enters its mature stage (cumulonimbi), the fragmentation in ice–ice collisions becomes even faster, contributing ~95% to the total ice formed in all SIP processes.

5. Summary and conclusions

A case of a squall line consisting of deep convective and trailing stratiform clouds, observed over Oklahoma on 11 May 2011, has been simulated with AC. This simulation adequately compares with the coincident aircraft and ground-based observations of the MCS from the MC3E (section 3a). In the vertical profiles, predicted averages of the filtered ice concentration (NI_{200}) and cloud droplet concentrations at all levels differ by less than 30% from the coincident aircraft observations for stratiform and convective regions in the storm. Previous modeling studies (e.g., Fridlind et al. 2017) have reported underprediction in the observed ice concentration (by about an order of magnitude) for the MC3E squall line. The present study has closed this gap between the predicted and observed ice concentrations. Also, domainwide averages of the TOA radiative fluxes have errors of less than about 30% at any instant both in the shortwave and longwave throughout the entire simulated period. This is consistent with the accuracy of predicted particle concentrations of droplets and ice because AC represents the dependency of radiative fluxes on particle size and concentration.

The budget analysis of total numbers of ice particles initiated shows that, for clouds with tops warmer than −36°C, fragmentation in ice–ice collisions dominates among all four SIP mechanisms [section 2b(2)]. As the simulated MC3E case is deep convection (cloud tops ~ −60°C) with abundant snow, graupel, or hail, the collisions between snow and graupel/hail and snow–snow collision contribute ~44% and 27%, respectively, to the total ice formed in fragmentation in ice–ice collisions. In this budget, only fragments from sublimational breakup that survived (about 20% of the true total) descent to reach the ascent are counted.

In the present study, the IE ratio is defined as the ratio between the number concentrations of total nonhomogeneously nucleated ice and active INP. Using this metric, following the progression of convective clouds growing to become cumulonimbi, the total intensity of ice multiplication and its balance of multiple SIP processes is predicted to evolve with the age of the clouds. Our simulation shows the dependency on cloud-top temperature of the IE ratio, which is typically between 10 and 10^3, and is dominated by the younger growing convective turrets. The corresponding contributions to this dependency from the SIP processes are diagnosed with dedicated tagging tracers. This explains the high concentrations of ice particles in young cumuli and mature clouds in MC3E.

The conclusions from the validated simulation of the MC3E storm are as follows:

1) Simulated IE ratios were between 10 and 10^3 for cloud tops between 0° and −30°C with a peak (10^3) at cloud tops of about −10°C and a minimum value (50) at −22°C. At most cloud-top temperatures, the IE ratios are about 10^2. Similar orders of magnitude for the IE ratio were observed by H80, who reported a peak at cloud-top temperatures close to −12°C.

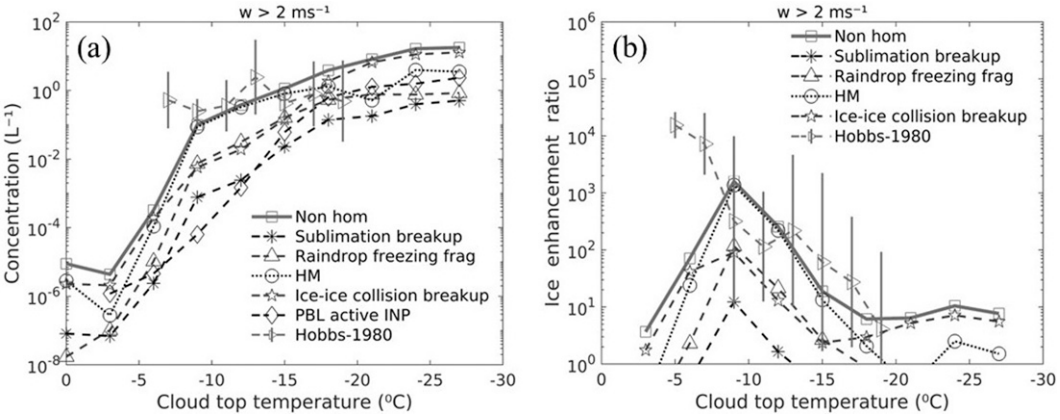

FIG. 18. (a) Predicted total nonhomogeneous ice (total ice from cloud ice and snow minus total homogeneous ice) (full line with squares) concentration is shown, as well as ice concentrations tracked by tracers (cloud ice + snow) from dendritic and graupel sublimation breakup (asterisks), fragmentation in raindrop freezing (upward-pointing triangles), the HM process (open circles), and fragmentation in the ice–ice collision (pentagrams), the PBL predicted active INP concentration (diamonds) in the convection and ice concentration observed by H80 (right-pointing triangles) as a function of cloud-top temperature. Also shown are (b) predicted ice enhancement ratios from total ice (cloud ice + snow) (full line with squares), and various tracers plotted as in (a) corresponding to these PBL-derived active INPs as a function of cloud-top temperature and compared with observed IE ratios by H80 (right-pointing triangles). Error bars are standard errors of ice concentration and IE ratios. All predicted ice concentrations were conditionally averaged over cloudy convective updrafts (>2 m s^{-1}). Geometric means of nonzero values of concentrations are shown here.

2) The predicted IE ratio decreases with decreasing cloud-top temperatures down to −22°C and is higher (10^4) for faster convective ascent and descent.
3) As expected for the relatively warm bases (17°C), the HM process of rime splintering dominates overall ice concentrations in young convective clouds (~15 min since cloud tops first rise above the freezing level). In contrast, fragmentation in ice–ice collisions prevails in the less young convective clouds with tops reaching above the −20°C level and for long times (>30–45 min) of MCS of multiple cells.
4) Regarding vertical profiles of tagging tracers averaged over the entire simulation, fragmentation in ice–ice collisions dominates overall ice concentrations above the −15°C level.
   (i) In convective updrafts and downdrafts, fragmentation in ice–ice collisions dominates the overall ice concentration and contributes about 70% to the concentrations of all secondary ice.
   (ii) Fragmentation during sublimation only occurs in downdrafts, where it is the second most dominant SIP mechanism, creating IE ratios of 10^2. In convective updrafts, it only contributes an IE ratio of about 10, which is much smaller than the total IE ratio.
5) During the evolution of the storm, the initial explosive growth of ice concentrations (cloud tops warmer than −15°C) of is due to the fast HM process and subsequent fragmentation in ice–ice collisions that prevails at longer times. The growth is slower for warmer cloud tops (warmer than −5°C). The HM process prevails in young cumulus turrets ascending into subzero levels (e.g., Yano and Phillips 2011).
6) The ranking of SIP mechanisms in order of importance, according to contributions to the predicted IE ratio as a function of cloud-top temperature, is as follows:
   (i) In young, growing convective clouds, the HM process can be ranked as the first, fragmentation in ice–ice collisions to be second, raindrop freezing fragmentation as the third and fragmentation during sublimation as the fourth most prolific SIP mechanism.
   (ii) In stratiform clouds, the dependency of IE ratio on cloud-top temperature is similar to that for convective clouds. Fragmentation in ice–ice collisions can

TABLE 3. List of various simulations performed with AC.

Run performed	Description
Control	Included all the SIP processes [section 2b(2)]
No HM case	HM process prohibited from the control run
No fragmentation in ice–ice collisions case	Fragmentation in ice–ice collisions process prohibited from the control run
No raindrop freezing fragmentation case	Raindrop freezing fragmentation process prohibited from the control run
No fragmentation during sublimation case	Fragmentation during sublimation is prohibited from the control run
No SIP case	All the SIP mechanisms were prohibited from the control run

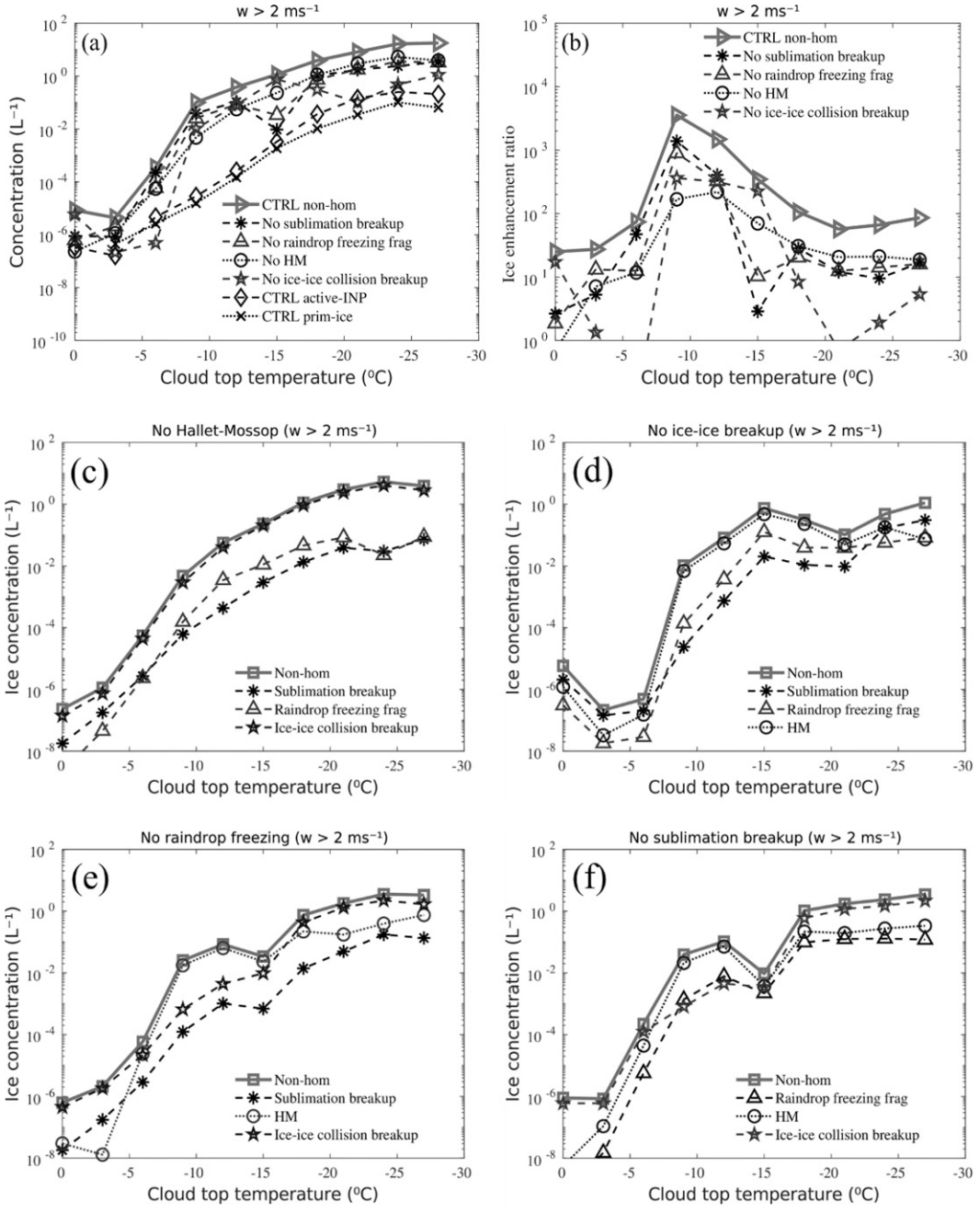

FIG. 19. Predicted active INPs, total nonhomogeneous ice (total ice from cloud ice and snow minus total homogeneous ice) concentrations, and IE ratio vs cloud-top temperature averaged over fast convective cloudy updrafts (>2 m s^{-1}) for the simulated MC3E case from the control run and sensitivity tests. (a) Concentrations of active INPs (diamonds) and nonhomogeneous ice (solid line with right-pointing triangles) from the control simulation, and nonhomogeneous ice concentrations from no sublimation breakup (asterisks), no raindrop freezing (upward-pointing triangles), no HM (open circles), and no fragmentation in ice–ice collisions (pentagrams). (b) Predicted IE ratio as a function of cloud-top temperatures for cloudy convective updrafts (>2 m s^{-1}) from the control and various sensitivity tests runs. Contribution in ice number concentration from tracers of individual SIP process in the absence of (c) the HM process, (d) fragmentation in ice–ice collisions, (e) raindrop freezing fragmentation, and (f) fragmentation during sublimation breakup. All concentrations are geometric means of the nonzero values.

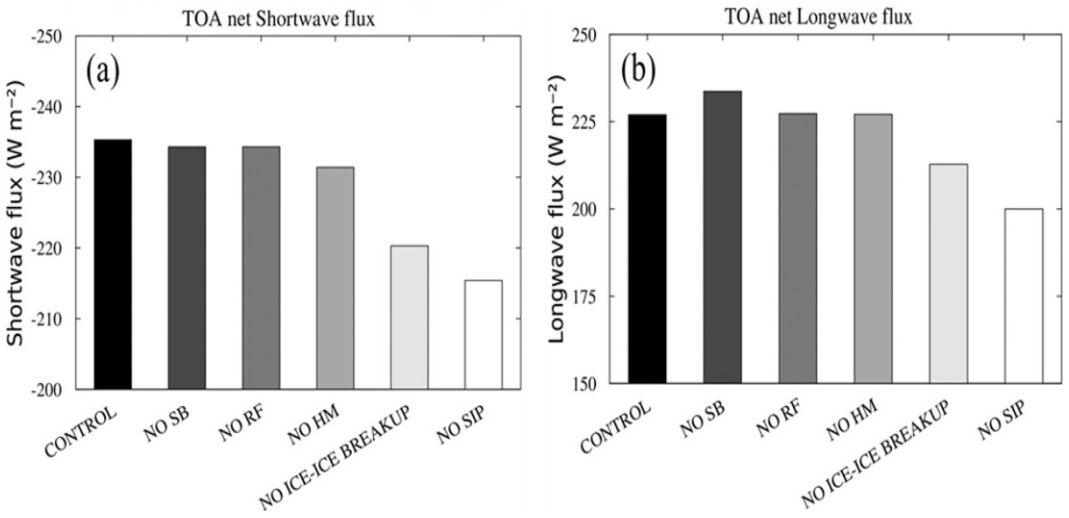

FIG. 20. The domain averaged TOA net (a) SW and (b) LW radiative flux from the control and various sensitivity tests runs (NO-SB: no sublimation breakup; NO-RF: no raindrop freezing fragmentation; NO-HM: no HM process; NO-ICE-ICE BREAKUP: no fragmentation in ice–ice collisions; and NO-SIP).

be ranked as the first most prolific SIP mechanism, the HM process as the second, fragmentation during sublimation as the third, and fragmentation during raindrop freezing as the fourth most prolific SIP mechanism.

(iii) In mature convective clouds with the coldest tops (Fig. 21b), the fragmentation in ice–ice collisions is the first most prolific SIP mechanism, whereas the HM process is the second, raindrop freezing fragmentation being the third and fragmentation during sublimation the fourth. This is consistent with fragmentation in ice–ice collisions being ubiquitous above the freezing level, without the restrictive conditions of the HM process.

7) There is a reduction in both SW (by about 8%) and LW (by about 12%) net radiative fluxes predicted at the TOA in the "no SIP" and no "fragmentation in ice–ice collisions" case relative to the control run. This is because of increasing cloud cover and LWC especially in the upper half of the mixed-phase region.
8) Most of the graupel is generated by the ice-crystal process with riming of snow. There is less contribution (by about 0.5–1 order of magnitude) to the total amount of graupel from the freezing of rain from the warm rain process (coalescence).
9) The predicted average ice concentration is never greater than the theoretical maximum for the onset of subsaturation with respect to liquid water at all levels warmer than about −30°C, where SIP is more prolific than homogeneous freezing. The order of magnitude is the same at most levels above −15°C so the theoretical maximum can be used as a rough approximation of total ice. This is explicable in terms of the explosive growth of ice particle number concentrations from ice multiplication ceasing shortly after the onset of subsaturation with respect to liquid, when the simulated mixed-phase cloud becomes "ice-only." This collapse of the humidity to near ice saturation inhibits both the vapor growth of fragments and all riming, preventing them from growing to become ice precipitation, and severing all positive feedbacks of ice multiplication by almost all of the SIP mechanisms, as theorized by Yano and Phillips (2011) (see also Phillips et al. 2017).

Regarding point 3, the young age of convective turrets sampled in past field studies explains why the HM process seemingly appeared to dominate ice concentrations in correlations from analysis of aircraft observations (Hallett et al. 1978; Harris-Hobbs and Cooper 1987; Blyth and Latham 1993). For example, Blyth and Latham (1993) report that ice concentrations were orders of magnitude lower when the conditions for the HM process were not met. In such field studies, their aircraft preferentially sampled younger clouds. The different rankings of SIP mechanisms depending on cloud age between points 3 and 4 suggests the importance of sampling convective clouds in a manner that is irrespective of their age in aircraft campaigns.

Under suitable conditions (−3° to −8°C and cloud droplets > 24 μm), HM splinters are predicted to form from graupel with a typical onset time of 10–15 min and the typical onset time of fragmentation in ice–ice collisions is predicted to be 45 min. This is consistent with the theory (Yano and Phillips 2011). In deep convective clouds, raindrop freezing fragmentation can accelerate fragmentation in ice–ice collisions by reducing its onset time, because collisions between ice crystals and supercooled rain immediately form large graupel (Phillips et al. 2001). It can also radically reduce the time required for the onset of the HM process (Phillips et al. 2001, 2002). Splinters formed in all SIP mechanisms can be either upwelled or downwelled (sublimation breakup) to higher or lower levels in the cloud. So, the most likely SIP mechanism responsible

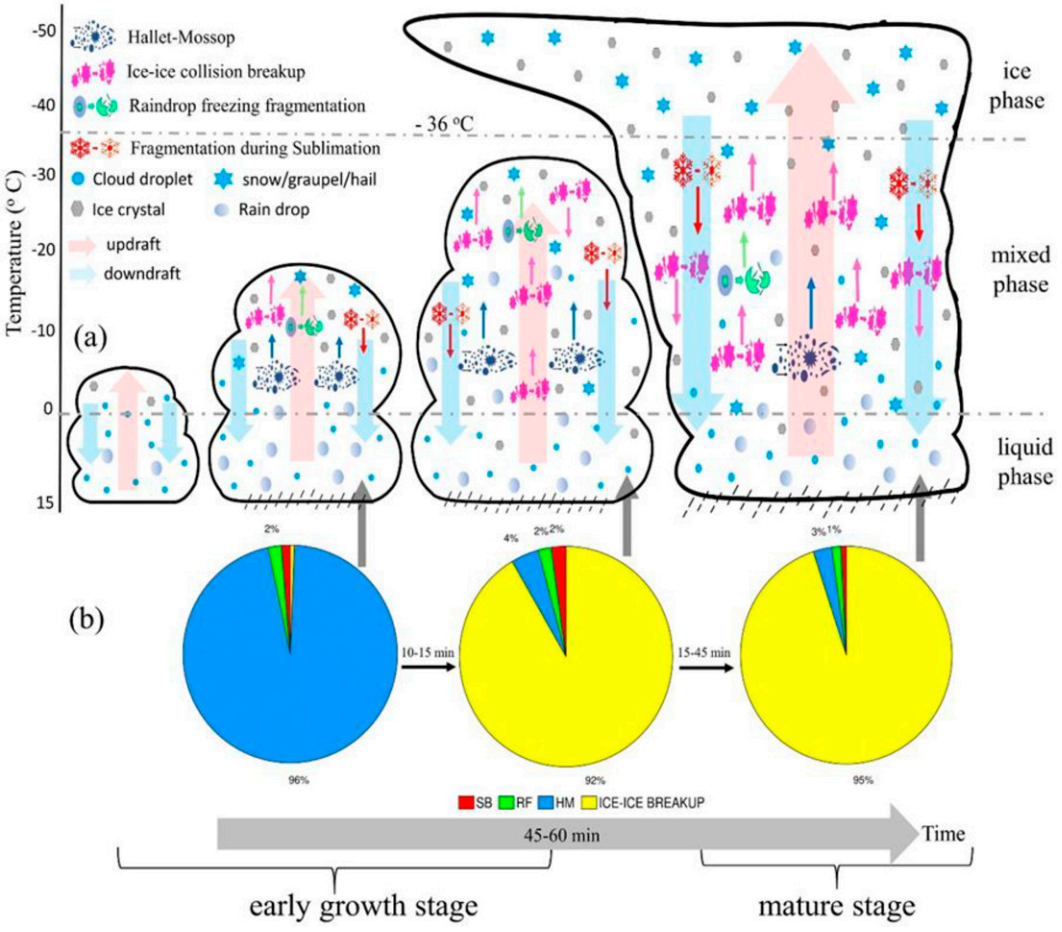

FIG. 21. (a) The schematic cloud structure in MC3E with cloud top growing from −5° to −50°C from the control simulation showing different SIP mechanisms active and vertical velocity (shown with upward- and downward-pointing arrows). Upwelling (downwelling) of the splinters formed is shown with a small upward (downward)-pointing arrow on top (bottom) of each SIP process. (b) Pie chart showing the relative contribution of various SIP mechanisms (SB: fragmentation in sublimation of ice; RF: fragmentation in raindrop freezing; HM: the HM process; and ICE–ICE BREAKUP: fragmentation in ice–ice collisions) to the total ice formed in all secondary processes for each cloud shown in (a). The time arrow at the bottom indicates the typical time required for the cloud to reach in mature stage from its early growth stage.

for the peak in IE ratio observed by H80 near a cloud-top temperature of −12°C is the HM process, because such clouds sampled by them were relatively young.

Currently, most numerical models consider only the HM process of rime splintering as representative of SIP in natural clouds. The present study suggests that SIP in warm-based young, convective clouds in their early growth stage (tops above the freezing level) can be attributed mainly to the HM process. However, the HM process is active only in a narrow temperature range (−3° to −8°C). Moreover, the mean droplet size is often insufficient for the observed ice enhancement to be accounted for by the HM process. This enhancement is seen to be several orders of magnitude aloft in natural convective clouds that are developing (e.g., cumulus congestus) or mature (e.g., cumulonimbi). The HM process can be inactive in cold-based, mixed-phase clouds (Morrison et al. 2005; Yano and Phillips 2011), such as those in the polar regions, and in clouds with scarce availability of larger cloud drops (Phillips et al. 2017b; Sotiropoulou et al. 2020; Zhao et al. 2021). In such clouds, the explosive growth of ice crystals can be governed by other SIP mechanisms (section 1a). Here our AC simulations reveal that, along with the HM process, several other SIP mechanisms must be active in the simulated MCS case, causing such high ice concentrations (10^2–10^3 L^{-1}) observed by the aircraft.

Regarding the ranking of SIP mechanisms (point 6 and 7), all the analysis with sensitivity tests (section 4) and with tagging tracers (section 3b) shows that the fragmentation in ice–ice collisions makes the maximum contribution (>75%) to the total ice below the −36°C level. Thus, fragmentation in ice–ice collisions is essential for accuracy of predicted ice concentrations aloft in the upper half of the mixed-phase region. This indicates that the HM process alone cannot create the high ice concentrations typically seen (~10^2–10^3 L^{-1}),

especially in deep convective clouds (e.g., cumulonimbi), in the present MC3E case.

Generally, the raindrop freezing fragmentation (Rangno 2008; Phillips et al. 2018) can be a prolific SIP mechanism, especially in maritime or tropical deep convective clouds, if larger cloud drops are present. Yet, in the present study, the high CCN concentrations (~2000 cm^{-3}, Fig. 4a) inhibit the warm rain process despite the warm cloud base, so that raindrop freezing fragmentation is less prolific and only ranked in third place overall. However, for warmer cloud tops (>−15°C), raindrop freezing fragmentation shares the joint second place with fragmentation in ice–ice collisions, creating IE ratios as high as 10^2. Subsequently, the fragmentation during sublimation can significantly contribute to the total ice, especially in stronger downdrafts (<−4 m s^{-1}, Fig. 12a).

The upwelling of large snow and graupel into the upper half of the mixed-phase region results in copious fragmentation in ice–ice collisions (section 3b). The predicted budget of fragmentation in ice–ice collisions strongly depends on vertical velocity for the stratiform versus convective contrast, more so than on temperature. Most (~70%) splinters from fragmentation in ice–ice collisions are emitted in weak or moderate convective ascent (<10 m s^{-1}) and in the upper half of the mixed-phase region (<−20°C). This is consistent with total ice concentrations in ascending cloud tops above the −16°C level being driven mainly by fragmentation in ice–ice collisions, because such cloud-top regions have had at least 10 min of prior glaciation for this slower yet persistent process to prevail, relative to the HM process (accelerated by collisional raindrop freezing).

To conclude, this study predicts the classic dependency observed by H80 (Fig. 25 therein) of IE ratio on cloud-top temperature in young convective turrets (Fig. 1). In our simulation of similar summertime deep convection (2011) in the continental United States, two SIP mechanisms (the HM process and fragmentation in ice–ice collisions) are responsible for the explosive growth of ice concentrations in convective ascent and descent, accounting for this pattern of IE ratio. The prediction includes the same observed peak from H80 (in the vicinity of about −12°C of cloud-top temperature) in terms of upwelled splinters from the HM process, accelerated by raindrop freezing in collisions between supercooled raindrops and the HM splinters. The present study also concludes that the age of a cloud as it goes through its life cycle is of paramount importance for the relative balance of activities among the various mechanisms of SIP.

Finally, it is the concerted combination of multiple SIP mechanisms represented here that together accurately explains the observed disparity between concentrations of ice and INPs in our simulated line of convection (Fig. 8). Dependencies of these SIP mechanisms on quantities, such as droplet size, temperature, vertical velocity, and hydrometeor fall speed, make their relative importance for ice initiation differ among different cloud types. This highlights the need for continued innovation of new laboratory experiments and theoretical representations of various SIP mechanisms (section 1a) to inform formulations in atmospheric models. This is especially true for breakup in collisions among ice particles.

Acknowledgments. The project was funded mainly through a research grant to Vaughan Phillips (VTJP) from the Swedish Research Council for Sustainable Development ("FORMAS" Award 2018-01795), which supported the first author. This award concerns the effects on clouds and climate arising from the time dependence of ice initiation. VTJP planned and directed the present study. Also, coauthors at Lund were supported by awards to VTJP from the U.S. Department of Energy (DOE) (DE-SC0018932), about ice initiation in clouds, from the Swedish Research Council ("Vetenskapsradet") about bioaerosol effects on clouds and from the U.S. DOE (DE-SC0018967) with a subaward from the University of Oklahoma about reasons for high concentrations of ice in clouds. Paul DeMott participated through the support of the Atmospheric System Research Program of the DOE Office of Biological and Environmental Research, Climate and Environmental Science Division under Award DE-SC0021116. There are no competing interests.

Data availability statement. The "cloud-top algorithm" code is available from the corresponding author on a request. The data that support and are used in this study are also available on a request. The codes representing SIP in the cloud model are freely available on request.

APPENDIX

Cloud-Top Detection and Classification

The convective line observed in MC3E has been simulated by AC (section 2). The cloud-top temperature for the simulation is detected by our cloud-top detection algorithm. The algorithm is described as follows.

In the cloud-top algorithm, convective cores are first automatically identified using the partitioning method by Xu (1995). According to this method, a convective core satisfies one of the following four conditions:

(i) the horizontal distribution of maximum cloud draft strength below the melting level ($|w_{max}|$) is twice as large as the average over the four adjacent grid columns, or
(ii) $|w_{max}|$ is greater than 3 m s^{-1}, or
(iii) surface precipitation rate ($\langle P \rangle$) is greater than 25 mm h^{-1}, or
(iv) rain rate twice as greater as the average taken over the surrounding four grid points ($\langle P \rangle$) (Tao and Simpson 1989).

Grid columns other than the convective core and for which the total liquid water path (TLWP) is positive were chosen as convective grid columns. A region including a core and immediately adjacent convective grid columns is then defined as a convective region following Tao and Simpson (1989). The grid columns where TLWP exceeds 0.2 kg m^{-2} were identified as stratiform regions, and the remaining grid columns were defined as clear regions.

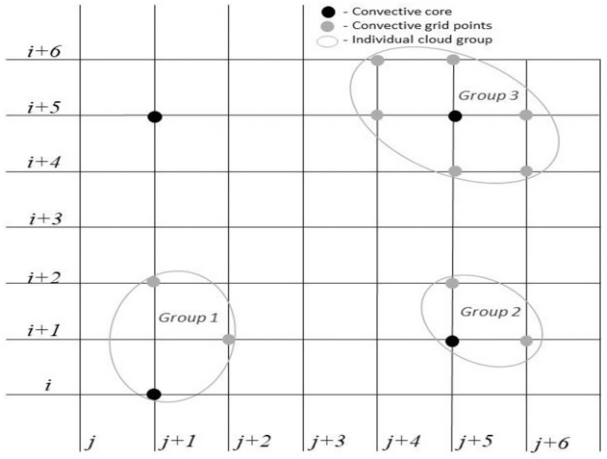

FIG. A1. Schematic diagram representing cloud grouping in the control simulation of AC. Filled black circles are cores, and filled gray circles represents convective grids adjacent to an individual core.

a. Step 1: Instantaneous grouping of grid points

Once the convective region (core and adjacent convective columns) was identified, links between pairs of convective adjacent grid points were established at any given time. These links were then used to expand each convective region. Such links of grid points were then stored in individual cloud groups. For example, group 1 consist of a core and two convective grids where a core at $(i, j + 1)$ creates a link with a convective grid at $(i + 1, j + 2)$ and this convective grid can be linked to another convective grid at $(i + 2, j + 1)$ as shown in Fig. A1.

b. Step 2: Iterative grouping

A convective region may split into more convective regions as clouds evolve with time in the simulation. This splitting then later forms "extra clouds." This was done by defining "spatial–temporal links" between pairs of convective grid points [abs(w) > 1 m s^{-1}] that are adjacent in the spatial–temporal sense (in 4D). Clusters of contiguous spatial–temporal links in space–time were grouped.

c. Step 3: True cloud groups

A problem now arose that the expanded convective regions may have overlapped even though they are different clouds. So, there can be multiple clouds for a given convective region formed in steps 1 and 2. Consequently, we partitioned all the convective regions into distinct "sub–cloudy regions." To avoid overlapping convective regions found in step 2, two subgroups of convective regions were defined for a given time instance. If the grid points of these two subgroups were the same, they were said to be overlapped, and if not, then there was no overlap at a given time. These no-overlapped "sub–cloudy regions" are stored in "true cloud" groups.

d. Step 4: Actual cloud

Once the "true cloud" grid points (regions) associated with a core were found, convective columns in such a core were collected along with the convective grids adjacent to these columns to form an actual cloud shown in Fig. 21a.

REFERENCES

Bacon, N. J., B. D. Swanson, M. B. Baker, and E. J. Davis, 1998: Breakup of levitated frost particles. *J. Geophys. Res.*, **103**, 13 763–13 775, https://doi.org/10.1029/98JD01162.

Blakeslee, R., J. Hall, M. Goodman, P. Parker, L. Freudinger, and M. He, 2007: The Real Time Mission Monitor: A situational awareness tool for managing experiment assets. *NASA Science Technology Conf.*, College Park, MD, NASA.

Blyth, A. M., and J. Latham, 1993: Development of ice and precipitation in New Mexican summertime cumulus clouds. *Quart. J. Roy. Meteor. Soc.*, **119**, 91–120, https://doi.org/10.1002/qj.49711950905.

——, and ——, 1997: A multi-thermal model of cumulus glaciation via the Hallett-Mossop process. *Quart. J. Roy. Meteor. Soc.*, **123**, 1185–1198, https://doi.org/10.1002/qj.49712354104.

——, R. E. Benestad, P. R. Krehbiel, and J. Latham, 1997: Observations of supercooled raindrops in New Mexico summertime cumuli. *J. Atmos. Sci.*, **54**, 569–575, https://doi.org/10.1175/1520-0469(1997)054<0569:OOSRIN>2.0.CO;2.

Braga, R. C., and Coauthors, 2017: Further evidence for CCN aerosol concentrations determining the height of warm rain and ice initiation in convective clouds over the Amazon basin. *Atmos. Chem. Phys.*, **17**, 14 433–14 456, https://doi.org/10.5194/acp-17-14433-2017.

Cantrell, W., and A. Heymsfield, 2005: Production of ice in tropospheric clouds: A review. *Bull. Amer. Meteor. Soc.*, **86**, 795–808, https://doi.org/10.1175/BAMS-86-6-795.

Chin, M., R. B. Rood, S.-J. Lin, J.-F. Müller, and A. M. Thompson, 2000: Atmospheric sulfur cycle simulated in the global model GOCART: Model description and global properties. *J. Geophys. Res.*, **105**, 24 671–24 687, https://doi.org/10.1029/2000JD900384.

Chouippe, A., M. Krayer, M. Uhlmann, J. Dušek, A. Kiselev, and T. Leisner, 2019: Heat and water vapor transfer in the wake of a falling ice sphere and its implication for secondary ice formation in clouds. *New J. Phys.*, **21**, 043043, https://doi.org/10.1088/1367-2630/ab0a94.

Crawford, I., and Coauthors, 2012: Ice formation and development in aged, wintertime cumulus over the UK: Observations and modelling. *Atmos. Chem. Phys.*, **12**, 4963–4985, https://doi.org/10.5194/acp-12-4963-2012.

Cui, Z., S. Davies, K. S. Carslaw, and A. M. Blyth, 2011: The response of precipitation to aerosol through riming and melting in deep convective clouds. *Atmos. Chem. Phys.*, **11**, 3495–3510, https://doi.org/10.5194/acp-11-3495-2011.

DeMott, P. J., D. J. Cziczo, A. J. Prenni, D. M. Murphy, S. M. Kreidenweis, D. S. Thomson, R. Borys, and D. C. Rogers, 2003: Measurements of the concentration and composition of nuclei for cirrus formation. *Proc. Natl. Acad. Sci. USA*, **100**, 14 655–14 660, https://doi.org/10.1073/pnas.2532677100.

——, and Coauthors, 2015: Integrating laboratory and field data to quantify the immersion freezing ice nucleation activity of mineral dust particles. *Atmos. Chem. Phys.*, **15**, 393–409, https://doi.org/10.5194/acp-15-393-2015.

Deshmukh, A., V. T. J. Phillips, A. Bansemer, S. Patade, and D. Waman, 2022: New empirical formulation for the

sublimational breakup of graupel and dendritic snow. *J. Atmos. Sci.*, **79**, 317–336, https://doi.org/10.1175/JAS-D-20-0275.1.

Dong, Y. Y., and J. Hallett, 1989: Droplet accretion during rime growth and the formation of secondary ice crystals. *Quart. J. Roy. Meteor. Soc.*, **115**, 127–142, https://doi.org/10.1002/qj.49711548507.

——, R. G. Oraltay, and J. Hallett, 1994: Ice particle generation during evaporation. *Atmos. Res.*, **32**, 45–53, https://doi.org/10.1016/0169-8095(94)90050-7.

Dye, J. E., and P. V. Hobbs, 1968: The influence of environmental parameters on the freezing and fragmentation of suspended water drops. *J. Atmos. Sci.*, **25**, 82–96, https://doi.org/10.1175/1520-0469(1968)025<0082:TIOEPO>2.0.CO;2.

Eidhammer, T., and Coauthors, 2010: Ice initiation by aerosol particles: Measured and predicted ice nuclei concentrations versus measured ice crystal concentrations in an orographic wave cloud. *J. Atmos. Sci.*, **67**, 2417–2436, https://doi.org/10.1175/2010JAS3266.1.

Feng, Z., X. Dong, B. Xi, C. Schumacher, P. Minnis, and M. Khaiyer, 2011: Top-of-atmosphere radiation budget of convective core/stratiform rain and anvil clouds from deep convective systems. *J. Geophys. Res.*, **116**, D23202, https://doi.org/10.1029/2011JD016451.

Field, P. R., and A. J. Heymsfield, 2015: Importance of snow to global precipitation. *Geophys. Res. Lett.*, **42**, 9512–9520, https://doi.org/10.1002/2015GL065497.

——, ——, and A. Bansemer, 2006: Shattering and particle interarrival times measured by optical array probes in ice clouds. *J. Atmos. Oceanic Technol.*, **23**, 1357–1371, https://doi.org/10.1175/JTECH1922.1.

——, and Coauthors, 2017: Secondary ice production: Current state of the science and recommendations for the future. *Ice Formation and Evolution in Clouds and Precipitation: Measurement and Modeling Challenges*, *Meteor. Monogr.*, No. 58, Amer. Meteor. Soc., https://doi.org/10.1175/AMSMONOGRAPHS-D-16-0014.1.

Fridlind, A. M., A. S. Ackerman, G. McFarquhar, G. Zhang, M. R. Poellot, P. J. DeMott, A. J. Prenni, and A. J. Heymsfield, 2007: Ice properties of single-layer stratocumulus during the Mixed-Phase Arctic Cloud Experiment: 2. Model results. *J. Geophys. Res.*, **112**, D24202, https://doi.org/10.1029/2007JD008646.

——, and Coauthors, 2017: Derivation of aerosol profiles for MC3E convection studies and use in simulations of the 20 May squall line case. *Atmos. Chem. Phys.*, **17**, 5947–5972, https://doi.org/10.5194/acp-17-5947-2017.

Gayatri, K., S. Patade, J. Fan, and T. Prabhakaran, 2022: Pathways of precipitation formation in different thermodynamic and aerosol environments over the Indian Peninsula. *Atmos. Res.*, **266**, 105934, https://doi.org/10.1016/j.atmosres.2021.105934.

Georgakaki, P., G. Sotiropoulou, E. Vignon, A.-C. Billault-Roux, A. Berne, and A. Nenes, 2022: Secondary ice production processes in wintertime Alpine mixed-phase clouds. *Atmos. Chem. Phys.*, **22**, 1965–1988, https://doi.org/10.5194/acp-22-1965-2022.

Griggs, D. J., and T. W. Choularton, 1983: Freezing modes of riming droplets with application to ice splinter production. *Quart. J. Roy. Meteor. Soc.*, **109**, 243–253, https://doi.org/10.1002/qj.49710945912.

Gurganus, C., and P. Lawson, 2018: Laboratory and flight tests of 2D imaging probes: Toward a better understanding of instrument performance and the impact on archived data. *J. Atmos. Oceanic Technol.*, **35**, 1533–1553, https://doi.org/10.1175/JTECH-D-17-0202.1.

Hallett, J., and S. C. Mossop, 1974: Production of secondary ice particles during the riming process. *Nature*, **249**, 26–28, https://doi.org/10.1038/249026a0.

——, R. I. Sax, D. Lamb, and A. S. R. Murty, 1978: Aircraft measurements of ice in Florida cumuli. *Quart. J. Roy. Meteor. Soc.*, **104**, 631–651, https://doi.org/10.1002/qj.49710444108.

Harris-Hobbs, R. L., and W. A. Cooper, 1987: Field evidence supporting quantitative predictions of secondary ice production rates. *J. Atmos. Sci.*, **44**, 1071–1082, https://doi.org/10.1175/1520-0469(1987)044<1071:FESQPO>2.0.CO;2.

Heymsfield, A., and P. Willis, 2014: Cloud conditions favoring secondary ice particle production in tropical maritime convection. *J. Atmos. Sci.*, **71**, 4500–4526, https://doi.org/10.1175/JAS-D-14-0093.1.

Hobbs, P. V., 1969: Ice multiplication in clouds. *J. Atmos. Sci.*, **26**, 315–318, https://doi.org/10.1175/1520-0469(1969)026<0315:IMIC>2.0.CO;2.

——, 1972: Fragmentation of ice particles in clouds. *J. Rech. Atmos.*, **6**, 245–258.

——, and Coauthors, 1971: Studies of winter cyclonic storms over the Cascade Mountains (1970–71). University of Washington Dept. of Atmospheric Sciences Rep. VI, 312 pp.

——, M. K. Politovich, and L. F. Radke, 1980: The structures of summer convective clouds in eastern Montana. I: Natural clouds. *J. Appl. Meteor.*, **19**, 645–663, https://doi.org/10.1175/1520-0450(1980)019<0645:TSOSCC>2.0.CO;2.

Hong, Y., G. Liu, and J.-L. F. Li, 2016: Assessing the radiative effects of global ice clouds based on *CloudSat* and *CALIPSO* measurements. *J. Climate*, **29**, 7651–7674, https://doi.org/10.1175/JCLI-D-15-0799.1.

Huang, Y., A. M. Blyth, P. R. A. Brown, T. W. Choularton, and Z. Cui, 2017: Factors controlling secondary ice production in cumulus clouds. *Quart. J. Roy. Meteor. Soc.*, **143**, 1021–1031, https://doi.org/10.1002/qj.2987.

Jackson, R., J. R. French, D. C. Leon, D. M. Plummer, S. Lasher-Trapp, A. M. Blyth, and A. Korolev, 2018: Observations of the microphysical evolution of convective clouds in the southwest of the United Kingdom. *Atmos. Chem. Phys.*, **18**, 15 329–15 344, https://doi.org/10.5194/acp-18-15329-2018.

James, R. L., V. T. J. Phillips, and P. J. Connolly, 2021: Secondary ice production during the break-up of freezing water drops on impact with ice particles. *Atmos. Chem. Phys.*, **21**, 18 519–18 530, https://doi.org/10.5194/acp-21-18519-2021.

Jefferson, A., 2011: Aerosol Observing System (AOS) handbook. ARM Tech. Rep. ARM-TR-014, 32 pp, https://www.arm.gov/publications/tech_reports/handbooks/aos_handbook.pdf.

Jensen, M. P., and Coauthors, 2016: The Midlatitude Continental Convective Clouds Experiment (MC3E). *Bull. Amer. Meteor. Soc.*, **97**, 1667–1686, https://doi.org/10.1175/BAMS-D-14-00228.1.

Johnson, D. A., and J. Hallett, 1968: Freezing and shattering of supercooled water drops. *Quart. J. Roy. Meteor. Soc.*, **94**, 468–482, https://doi.org/10.1002/qj.49709440204.

Keinert, A., D. Spannagel, T. Leisner, and A. Kiselev, 2020: Secondary ice production upon freezing of freely falling drizzle droplets. *J. Atmos. Sci.*, **77**, 2959–2967, https://doi.org/10.1175/JAS-D-20-0081.1.

King, W. D., and N. H. Fletcher, 1976a: Thermal shock as an ice multiplication mechanism. Part I. Theory. *J. Atmos. Sci.*, **33**, 85–96, https://doi.org/10.1175/1520-0469(1976)033<0085:TSAAIM>2.0.CO;2.

——, and ——, 1976b: Thermal shock as an ice multiplication mechanism. Part II. Experimental. *J. Atmos. Sci.*, **33**, 97–102, https://doi.org/10.1175/1520-0469(1976)033<0097:TSAAIM>2.0.CO;2.

Kinne, S., and K.-N. Liou, 1989: The effects of the nonsphericity and size distribution of ice crystals on the radiative properties of cirrus clouds. *Atmos. Res.*, **24**, 273–284, https://doi.org/10.1016/0169-8095(89)90049-5.

Korolev, A. V., and I. P. Mazin, 2003: Supersaturation of water vapor in clouds. *J. Atmos. Sci.*, **60**, 2957–2974, https://doi.org/10.1175/1520-0469(2003)060<2957:SOWVIC>2.0.CO;2.

——, E. F. Emery, J. W. Strapp, S. G. Cober, G. A. Isaac, M. Wasey, and D. Marcotte, 2011: Small ice particles in tropospheric clouds: Fact or artifact? Airborne Icing Instrumentation Evaluation Experiment. *Bull. Amer. Meteor. Soc.*, **92**, 967–973, https://doi.org/10.1175/2010BAMS3141.1.

Kudzotsa, I., and Coauthors, 2016: Aerosol indirect effects on glaciated clouds. Part I: Model description. *Quart. J. Roy. Meteor. Soc.*, **142**, 1958–1969, https://doi.org/10.1002/qj.2791.

Ladino, L. A., A. Korolev, I. Heckman, M. Wolde, A. M. Fridlind, and A. S. Ackerman, 2017: On the role of ice-nucleating aerosol in the formation of ice particles in tropical mesoscale convective systems. *Geophys. Res. Lett.*, **44**, 1574–1582, https://doi.org/10.1002/2016GL072455.

Langmuir, I., 1948: The production of rain by a chain reaction in cumulus clouds at temperatures above freezing. *J. Atmos. Sci.*, **5**, 175–192, https://doi.org/10.1175/1520-0469(1948)005<0175:TPORBA>2.0.CO;2.

Lasher-Trapp, S., D. C. Leon, P. J. DeMott, C. M. Villanueva-Birriel, A. V. Johnson, D. H. Moser, C. S. Tully, and W. Wu, 2016: A multisensor investigation of rime splintering in tropical maritime cumuli. *J. Atmos. Sci.*, **73**, 2547–2564, https://doi.org/10.1175/JAS-D-15-0285.1.

——, E. L. Scott, E. Järvinen, M. Schnaiter, F. Waitz, P. J. DeMott, C. S. McCluskey, and T. C. J. Hill, 2021: Observations and modeling of rime splintering in Southern Ocean cumuli. *J. Geophys. Res. Atmos.*, **126**, e2021JD035479, https://doi.org/10.1029/2021JD035479.

Lawson, R. P., S. Woods, and H. Morrison, 2015: The microphysics of ice and precipitation development in tropical cumulus clouds. *J. Atmos. Sci.*, **72**, 2429–2445, https://doi.org/10.1175/JAS-D-14-0274.1.

Leisner, T., T. Pander, P. Handmann, and A. Kiselev, 2014: Secondary ice processes upon heterogeneous freezing of cloud droplets. *14th Conf. on Cloud Physics and Atmospheric Radiation*, Boston, MA, Amer. Meteor. Soc., 2.3, https://ams.confex.com/ams/14CLOUD14ATRAD/webprogram/Paper250221.html.

Lloyd, G., and Coauthors, 2020: Small ice particles at slightly supercooled temperatures in tropical maritime convection. *Atmos. Chem. Phys.*, **20**, 3895–3904, https://doi.org/10.5194/acp-20-3895-2020.

Ming, Y., V. Ramaswamy, L. J. Donner, and V. T. J. Phillips, 2006: A new parameterization of cloud droplet activation applicable to general circulation models. *J. Atmos. Sci.*, **63**, 1348–1356, https://doi.org/10.1175/JAS3686.1.

Möhler, O., and Coauthors, 2005: Effect of sulfuric acid coating on heterogeneous ice nucleation by soot aerosol particles. *J. Geophys. Res.*, **110**, D11210, https://doi.org/10.1029/2004JD005169.

Morrison, H., J. A. Curry, M. D. Shupe, and P. Zuidema, 2005: A new double-moment microphysics parameterization for application in cloud and climate models. Part II: Single-column modeling of Arctic clouds. *J. Atmos. Sci.*, **62**, 1678–1693, https://doi.org/10.1175/JAS3447.1.

Oraltay, R. G., and J. O. H. N. Hallett, 1989: Evaporation and melting of ice crystals: A laboratory study. *Atmos. Res.*, **24**, 169–189, https://doi.org/10.1016/0169-8095(89)90044-6.

Patade, S., S. Shete, N. Malap, G. Kulkarni, and T. V. Prabha, 2016: Observational and simulated cloud microphysical features of rain formation in the mixed phase clouds observed during CAIPEEX. *Atmos. Res.*, **169**, 32–45, https://doi.org/10.1016/j.atmosres.2015.09.018.

——, and Coauthors, 2021: Empirical formulation for multiple groups of primary biological ice nucleating particles from field observations over Amazonia. *J. Atmos. Sci.*, **78**, 2195–2220, https://doi.org/10.1175/JAS-D-20-0096.1.

Pauluis, O., and S. Garner, 2006: Sensitivity of radiative-convective equilibrium simulations to horizontal resolution. *J. Atmos. Sci.*, **63**, 1910–1923, https://doi.org/10.1175/JAS3705.1.

Phillips, V. T. J., 2021: Ice multiplication by fragmentation during quasi-spherical freezing of raindrops: A theoretical investigation. *J. Atmos. Sci.*, **78**, 3215–3228, https://doi.org/10.1175/JAS-D-20-0309.1.

——, A. M. Blyth, P. R. A. Brown, T. W. Choularton, and J. Latham, 2001: The glaciation of a cumulus cloud over New Mexico. *Quart. J. Roy. Meteor. Soc.*, **127**, 1513–1534, https://doi.org/10.1002/qj.49712757503.

——, T. W. Choularton, A. M. Blyth, and J. Latham, 2002: The influence of aerosol concentrations on the glaciation and precipitation of a cumulus cloud. *Quart. J. Roy. Meteor. Soc.*, **128**, 951–971, https://doi.org/10.1256/0035900021643601.

——, L. J. Donner, and S. T. Garner, 2007: Nucleation processes in deep convection simulated by a cloud-system-resolving model with double-moment bulk microphysics. *J. Atmos. Sci.*, **64**, 738–761, https://doi.org/10.1175/JAS3869.1.

——, P. J. DeMott, and C. Andronache, 2008: An empirical parameterization of heterogeneous ice nucleation for multiple chemical species of aerosol. *J. Atmos. Sci.*, **65**, 2757–2783, https://doi.org/10.1175/2007JAS2546.1.

——, and Coauthors, 2009: Potential impacts from biological aerosols on ensembles of continental clouds simulated numerically. *Biogeosciences*, **6**, 987–1014, https://doi.org/10.5194/bg-6-987-2009.

——, P. J. Demott, C. Andronache, K. A. Pratt, K. A. Prather, R. Subramanian, and C. Twohy, 2013: Improvements to an empirical parameterization of heterogeneous ice nucleation and its comparison with observations. *J. Atmos. Sci.*, **70**, 378–409, https://doi.org/10.1175/JAS-D-12-080.1.

——, A. Khain, N. Benmoshe, E. Ilotoviz, and A. Ryzhkov, 2015: Theory of time-dependent freezing. Part II: Scheme for freezing raindrops and simulations by a cloud model with spectral bin microphysics. *J. Atmos. Sci.*, **72**, 262–286, https://doi.org/10.1175/JAS-D-13-0376.1.

——, J.-I. Yano, and A. Khain, 2017a: Ice multiplication by breakup in ice–ice collisions. Part I: Theoretical formulation. *J. Atmos. Sci.*, **74**, 1705–1719, https://doi.org/10.1175/JAS-D-16-0224.1.

——, and Coauthors, 2017b: Ice multiplication by breakup in ice–ice collisions. Part II: Numerical simulations. *J. Atmos. Sci.*, **74**, 2789–2811, https://doi.org/10.1175/JAS-D-16-0223.1.

——, S. Patade, J. Gutierrez, and A. Bansemer, 2018: Secondary ice production by fragmentation of freezing drops: Formulation and theory. *J. Atmos. Sci.*, **75**, 3031–3070, https://doi.org/10.1175/JAS-D-17-0190.1.

——, and Coauthors, 2020: Multiple environmental influences on the lightning of cold-based continental cumulonimbus clouds.

Part I: Description and validation of model. *J. Atmos. Sci.*, **77**, 3999–4024, https://doi.org/10.1175/JAS-D-19-0200.1.

Prabhakaran, P., G. Kinney, W. Cantrell, R. A. Shaw, E. Bodenschatz, 2019: Ice nucleation in the wake of warm hydrometeors. arXiv, 1906.06129, https://arxiv.org/abs/1906.06129.

——, A. S. M. Shawon, G. Kinney, S. Thomas, W. Cantrell, and R. A. Shaw, 2020: The role of turbulent fluctuations in aerosol activation and cloud formation. *Proc. Natl. Acad. Sci. USA*, **117**, 16 831–16 838, https://doi.org/10.1073/pnas.2006426117.

Pruppacher, H. R., and R. J. Schlamp, 1975: A wind tunnel investigation on ice multiplication by freezing of waterdrops falling at terminal velocity in air. *J. Geophys. Res.*, **80**, 380–386, https://doi.org/10.1029/JC080i003p00380.

——, and J. Klett, 1997: *Microphysics of Clouds and Precipitation.* 2nd ed. Atmospheric and Oceanographic Sciences Library, Vol. 18, Kluwer Academic, 954 pp.

Rangno, A. L., 2008: Fragmentation of freezing drops in shallow maritime frontal clouds. *J. Atmos. Sci.*, **65**, 1455–1466, https://doi.org/10.1175/2007JAS2295.1.

——, and P. V. Hobbs, 2001: Ice particles in stratiform clouds in the Arctic and possible mechanisms for the production of high ice concentrations. *J. Geophys. Res.*, **106**, 15 065–15 075, https://doi.org/10.1029/2000JD900286.

Saleeby, S. M., S. C. van den Heever, P. J. Marinescu, S. M. Kreidenweis, and P. J. DeMott, 2016: Aerosol effects on the anvil characteristics of mesoscale convective systems. *J. Geophys. Res. Atmos.*, **121**, 10 880–10 901, https://doi.org/10.1002/2016JD025082.

Sotiropoulou, G., S. Sullivan, J. Savre, G. Lloyd, T. Lachlan-Cope, A. M. Ekman, and A. Nenes, 2020: The impact of secondary ice production on Arctic stratocumulus. *Atmos. Chem. Phys.*, **20**, 1301–1316, https://doi.org/10.5194/acp-20-1301-2020.

——, É. Vignon, G. Young, H. Morrison, S. J. O'Shea, T. Lachlan-Cope, A. Berne, and A. Nenes, 2021: Secondary ice production in summer clouds over the Antarctic coast: An underappreciated process in atmospheric models. *Atmos. Chem. Phys.*, **21**, 755–771, https://doi.org/10.5194/acp-21-755-2021.

Sullivan, S. C., C. Hoose, and A. Nenes, 2017: Investigating the contribution of secondary ice production to in-cloud ice crystal numbers. *J. Geophys. Res. Atmos.*, **122**, 9391–9412, https://doi.org/10.1002/2017JD026546.

Sun, J., P. A. Ariya, H. G. Leighton, and M. K. Yau, 2012: Modeling study of ice formation in warm-based precipitating shallow cumulus clouds. *J. Atmos. Sci.*, **69**, 3315–3335, https://doi.org/10.1175/JAS-D-11-0344.1.

Takahashi, T., Y. Nagao, and Y. Kushiyama, 1995: Possible high ice particle production during graupel–graupel collisions. *J. Atmos. Sci.*, **52**, 4523–4527, https://doi.org/10.1175/1520-0469(1995)052<4523:PHIPPD>2.0.CO;2.

Tao, W.-K., and J. Simpson, 1989: Modeling study of a tropical squall-type convective line. *J. Atmos. Sci.*, **46**, 177–202, https://doi.org/10.1175/1520-0469(1989)046<0177:MSOATS>2.0.CO;2.

Uin, J., 2016: Cloud Condensation Nuclei Particle Counter (CCN) instrument handbook. ARM Rep. DOE/SC-ARM-TR-168, 16 pp.

Vardiman, L., 1978: The generation of secondary ice particles in clouds by crystal–crystal collision. *J. Atmos. Sci.*, **35**, 2168–2180, https://doi.org/10.1175/1520-0469(1978)035<2168:TGOSIP>2.0.CO;2.

Xie, S., Y. Zhang, S. E. Giangrande, M. P. Jensen, R. McCoy, and M. Zhang, 2014: Interactions between cumulus convection and its environment as revealed by the MC3E sounding array. *J. Geophys. Res. Atmos.*, **119**, 11 784–11 808, https://doi.org/10.1002/2014JD022011.

Xu, K.-M., 1995: Partitioning mass, heat, and moisture budgets of explicitly simulated cumulus ensembles into convective and stratiform components. *J. Atmos. Sci.*, **52**, 551–573, https://doi.org/10.1175/1520-0469(1995)052<0551:PMHAMB>2.0.CO;2.

Yang, J., H. Lei, Z. Hu, and T. Hou, 2014: Particle size spectra and possible mechanisms of high ice concentration in nimbostratus over Hebei Province, China. *Atmos. Res.*, **142**, 79–90, https://doi.org/10.1016/j.atmosres.2013.12.018.

Yano, J.-I., and V. T. J. Phillips, 2011: Ice–ice collisions: An ice multiplication process in atmospheric clouds. *J. Atmos. Sci.*, **68**, 322–333, https://doi.org/10.1175/2010JAS3607.1.

Yau, M. K., and R. R. Rogers, 1996: *A Short Course in Cloud Physics.* 3rd ed. Elsevier, 304 pp.

Young, G., T. Lachlan-Cope, S. J. O'Shea, C. Dearden, C. Listowski, K. N. Bower, T. W. Choularton, and M. W. Gallagher, 2019: Radiative effects of secondary ice enhancement in coastal Antarctic clouds. *Geophys. Res. Lett.*, **46**, 2312–2321, https://doi.org/10.1029/2018GL080551.

Zhao, X., and X. Liu, 2021: Global importance of secondary ice production. *Geophys. Res. Lett.*, **48**, e2021GL092581, https://doi.org/10.1029/2021GL092581.

——, ——, V. T. J. Phillips, and S. Patade, 2021: Impacts of secondary ice production on Arctic mixed-phase clouds based on ARM observations and CAM6 single-column model simulations. *Atmos. Chem. Phys.*, **21**, 5685–5703, https://doi.org/10.5194/acp-21-5685-2021.